

Full-F Turbulent Simulation in a Linear Plasma Device using a Gyro-Moment Approach

B. J. Frei,^{1,2} J. Mencke,¹ and P. Ricci¹

¹*Ecole Polytechnique Fédérale de Lausanne (EPFL), Swiss Plasma Center, CH-1015 Lausanne, Switzerland*

²*Max-Planck-Institut für Plasmaphysik, D-85748 Garching, Germany*

(*Electronic mail: baptiste.frei@ipp.mpg.de)

(Dated: 12 January 2024)

Simulations of plasma turbulence in a linear plasma device configuration are presented. These simulations are based on a simplified version of the gyrokinetic (GK) model proposed by B. J. Frei *et al.* [J. Plasma Phys. **86**, 905860205 (2020)] where the full-F distribution function is expanded on a velocity-space polynomial basis allowing us to reduce its evolution to the solution of an arbitrary number of fluid-like equations for the expansion coefficients, denoted as the gyro-moments (GM). By focusing on the electrostatic and neglecting finite Larmor radius effects, a full-F GM hierarchy equation is derived to evolve the ion dynamics, which includes a nonlinear Dougherty collision operator, localized sources, and Bohm sheath boundary conditions. An electron fluid Braginskii model is used to evolve the electron dynamics, coupled to the full-F ion GM hierarchy equation via a vorticity equation where the Boussinesq approximation is used. A set of full-F turbulent simulations are then performed using the parameters of the Large Plasma Device (LAPD) experiments with different numbers of ion GMs and different values of collisionality. The ion distribution function is analyzed illustrating the convergence properties of the GM approach. In particular, we show that higher-order GMs are damped by collisions in the high-collisional regime relevant to LAPD experiments. The GM results are then compared with those from two-fluid Braginskii simulations, finding qualitative agreement in the time-averaged profiles and statistical turbulent properties.

I. INTRODUCTION

Despite recent progress in the development of gyrokinetic (GK) codes, such as COGENT¹, Gkeyll², GENE-X^{3,4} and XGC⁵, extending the GK model from the core to the boundary remains challenging since it requires dealing with a wide range of collisionality, order-one fluctuations across various scales, complex magnetic field geometry, steep pressure gradients and the interaction of the plasma with the wall. As a consequence, less computationally demanding tools such as fluid simulations (see, e.g., Refs. 6–8) based on the drift-reduced Braginskii model⁹, are often used to simulate the plasma dynamics in the boundary. However, the Braginskii fluid approach remains limited to the highly collisional region of the boundary, namely the scrape-off layer (SOL) and cannot describe kinetic effects at lower collisionality.

To tackle the challenges of the boundary region, an approach is formulated in Ref. 10 based on the Hermite-Laguerre expansion of the full (full-F) distribution function, which leads to the evolution of an arbitrary number of expansion coefficients, referred to as the gyro-moments GMs. This approach features kinetic effects^{11–13}, which are absent in Braginskii-like fluid models, and collisional effects modeled using advanced collision operators^{13–17} with an arbitrary number of GMs. The ability to adjust the number of GMs with a simple closure by truncation removes the need for *ad-hoc* kinetic closures^{18,19} since the accuracy of the model can be improved by increasing arbitrarily the number of GMs and, therefore, the velocity-space resolution. So far, investigations based on the GM approach are limited to the δf regime (where only the *a priori* small deviation of the distribution function from thermal equilibrium is evolved²⁰) showing

convergence with a low number of GMs, in particular at high collisionality¹³. We notice that the first nonlinear δf simulations using advanced linearized collision operators have been recently performed^{17,21} and that a similar approach has also been implemented to perform δf turbulent calculations focusing on the core region^{22,23}. In this work, we present the first full-F turbulent results that is based on the GM approach using a flexible number of moments. In particular, we focus on simulations of plasma turbulence in a linear plasma device.

Linear plasma devices, such as LAPD²⁴, HelCat²⁵ and RAID²⁶, are experiments that allow for the investigation of basic plasma phenomena in a simplified magnetic geometry characterized by the absence of magnetic gradients, curvature, and shear^{24,26–29}. Despite their simplicity and the lack of kinetic effects such as trapped electrons, linear plasma devices share some of the most important physical processes that occur in the boundary of magnetic confinement devices. In fact, similar to the boundary, the turbulent dynamics in a linear plasma device result from the interplay of cross-field transport, parallel flows to the magnetic field, and plasma losses at the end plates where a sheath forms due to plasma-wall interactions. At the same time, the straight magnetic field lines in these devices facilitate the development of new modelling tools, compared to complex magnetic geometry characterizing the boundary of fusion devices. The modelling in these devices is also simplified by the perpendicular incidence of the magnetic field lines to the wall of the machine, which simplifies the sheath boundary model compared to an oblique incidence^{30–32} and by the low plasma temperatures comparable to typical SOL values (e.g., $T_i \lesssim T_e \sim 6$ eV in typical LAPD discharges³³), which are ideal for applying the full-F GM approach.

The low plasma temperature allows for a direct comparison

of the GM approach with validated fluid simulations^{29,34–36}, which have been considered because of the collisional conditions often met in, e.g., LAPD experiments. Moreover, we note that, in addition to fluid simulations, LAPD configuration was also chosen to perform the first full-F GK simulation in open field lines with the Gkeyll code that uses a discontinuous-Galerkin approach to discretize the velocity-space³⁷. LAPD turbulent simulations using the GK GENE code are also reported in Ref. 38 based on the same physical model. In both cases, the GK model used for the LAPD simulations neglects finite Larmor radius (FLR) effects and can, therefore, be considered equivalent to a drift-kinetic model. As a matter of fact, previous fluid and GK simulations of LAPD provide a comparison that make linear plasma devices an ideal testbed to perform the first full-F turbulent simulations using the GM approach with an arbitrary number of GMs.

In this work, we consider a simplified version of the full-F GM model derived in Ref. 10. Consistently with Refs. 37 and 38, we focus on the long-wavelength electrostatic limit of the GK model to describe the ion dynamics, with ion-ion collisions modeled using a simple nonlinear Dougherty³⁹ collision operator (similar to the one used in Refs. 37 and 38). In addition, we neglect FLR effects and we refer to our ion model as a GK model for consistency with previous works^{37,38}, but emphasize its similarity to a drift-kinetic ion model. On the other hand, electrons are assumed collisional, such that their dynamics can be approximated by the drift-reduced Braginskii model⁹. This is in contrast with respect to previous GK simulations where electrons are treated using the long-wavelength (without FLR effects) GK equation. Hence, our model can be considered as a hybrid kinetic-fluid model, with a GK ion and fluid electron description.

In contrast to previous GK simulations of linear devices^{37,38}, the ion GK equation is solved within the GM approach where the full ion distribution function F_i is expanded on a Hermite and Laguerre polynomial basis. A parallel (to the magnetic field) velocity-space coordinate shifted by the local ion parallel fluid velocity and the adiabatic invariant are used to describe efficiently sonic ion parallel flows near the end plates where the sheath forms. A full-F ion GM hierarchy equation for the expansion coefficients is then derived. The ion full-F GM hierarchy equation and the fluid electron model are coupled through a vorticity equation where the Boussinesq approximation is considered. To incorporate the losses at the end plates, Bohm sheath boundary conditions³¹ are implemented in the parallel direction, which are equivalent to the ones used in the previous Braginskii simulation of LAPD^{29,35}. Nonlinear simulations of LAPD are then performed with various numbers of GMs. For comparison, a set of nonlinear turbulent simulations are also performed using the two-fluid drift-reduced Braginskii equations⁹ (or simply Braginskii model), similarly to Refs. 29 and 35, and using a reduced cold-ion model derived from the full-F ion GM hierarchy.

The present results demonstrate that the full-F GM approach properly describes fluctuations in an open-field line geometry. In fact, a detailed analysis shows that turbulence, driven by a long perpendicular wavelength Kelvin-Helmholtz

(KH) instability, is in qualitative agreement with the Braginskii model. The importance of the KH instability in determining the radial turbulent transport in LAPD, as pointed out by Ref. 29, motivate the long-wavelength approximation and neglecting FLR effects in the present work. Our findings exhibit weak dependence on the number of GMs employed in the simulations and on the collisional regime. This is primarily due to the absence of significant kinetic effects in LAPD and the fluid nature of the KH instability, which governs radial turbulent transport and manifests itself at long perpendicular wavelengths. The analysis of the velocity-space representation of the ion distribution function demonstrates that the amplitude of the GMs decays rapidly with the order of the polynomial when collisions are considered. The present investigation also reveals that a simple closure based on the truncation of the GM hierarchy is sufficient in our case and has little effect on turbulence. It is important to note that the purpose of these simulations is not to achieve a highly-fidelity and realistic description of LAPD turbulence, but rather to establish confidence in the applicability of the GM approach in full-F turbulent calculations with a flexible number of GMs. Furthermore, a direct comparison with LAPD experimental data^{35,40} and with previous GK simulations^{37,38} falls outside the scope of our study, but will be addressed in future work.

We remark that the GM approach of Ref. 10 shares some similarities with previous (full-F or δf) gyrofluid models^{19,41–49}, where a fixed number of moments, usually up to the third-order velocity-space moments, are evolved as dynamical variables. These models can be considered as the limit of the GM approach where a finite number of moments is evolved and properly designed closures to mimic kinetic effects, such as Landau damping and FLR effects. Hence, the GM approach used in this work is similar to a full-F gyrofluid model without FLR effects when the number of moments is kept constant. Finally, although our model considers a closure by truncation, FLR closures at arbitrary perpendicular wavelengths^{49–51} and collisional closures^{48,52} for full-F gyrofluid models can also be considered with an arbitrary number of GMs.

The paper is structured as follows. In Sec. II, we derive the ion full-F GM hierarchy equation in a straight magnetic field and introduce the electron fluid model, as well as the two-fluid drift-reduced Braginskii model. The numerical implementation of the full-F GM hierarchy equation is detailed in Sec. III. The results of the first full-F GM turbulent simulations are presented in Sec. IV, which includes a detailed comparison with the Braginskii simulations and an analysis of the ion distribution function. We conclude in Sec. V. Appendix A reports on the derivation of the ion temperature equation at high collisionality using the GM approach.

II. LINEAR PLASMA DEVICE MODEL

In this section, we derive the full-F GM hierarchy equation for the ion dynamics by expanding the ion distribution function onto a Hermite and Laguerre polynomials basis. The hierarchy includes particle and energy sources and a simple

nonlinear long-wavelength Dougherty collision operator. The ion full-F GM hierarchy is derived by neglecting FLR effects from gyro-average and the difference between particle and gyrocenter fluid quantities, but includes long-wavelength approximation of the polarization density in the quasineutrality equation where the Boussinesq approximation is considered. Ultimately, this allows us to remove the complexities of FLR effects in full-F calculations using a flexible number of GMs. A reduced cold-ion model is also considered, for comparison purposes, which is obtained analytically from the full-F GM hierarchy in the cold-ion ($T_i = 0$) limit. For the electron dynamics, the Braginskii fluid equations are used to evolve the electron density n_e , parallel velocity $U_{\parallel e}$, and temperature T_e . A vorticity equation is derived using the Boussinesq approximation for the electrostatic potential ϕ , which couples the ion and electron models. Finally, we present the two-fluid Braginskii model.

The simple magnetic geometry in a linear plasma device allows us to introduce a simple coordinate system. In particular, assuming a rectangular shape of the linear device cross-section, we define the cartesian coordinate system (x, y, z) , such that the (x, y) coordinates describe the plane perpendicular to \mathbf{B} , while z is the coordinate along the magnetic field lines. The height and width of the perpendicular cross-section are L_x and L_y , respectively, and the length of the linear plasma device is L_z . The constant in time and uniform in space magnetic field can simply be written as $\mathbf{B} = \nabla \times \mathbf{A} = B\mathbf{z}$, where \mathbf{A} is the magnetic vector potential, which is constant in time, and \mathbf{z} is the unit vector pointing along the axis of the linear device.

This section is structured as follows. We describe the ion full-F model in Sec. II A and we derive the ion full-F GM hierarchy equation in Sec. II B. A presentation of the reduced cold-ion model is then obtained from the GM hierarchy equation in Sec. II C. The fluid electron model follows in Sec. II D and the vorticity equation is derived in Sec. II E. Sec. II F describes the two-fluid Braginskii model used for comparison purposes and, finally, Sec. II G details the Bohm sheath boundary conditions we use in our simulations.

A. Ion full-F model

Focusing on the electrostatic and neglecting FLR effects with constant and straight magnetic field lines, the ion one-form Γ_i^{10} expressed in the gyrocenter coordinates $\mathbf{Z} = (\mathbf{R}_g, \mu, v_{\parallel}, \theta)$, where \mathbf{R}_g is the gyrocenter position, $\mu = m_i v_{\perp}^2 / (2B)$ is the magnetic moment and $v_{\parallel} = \mathbf{b} \cdot \mathbf{v}$ is the velocity parallel to the magnetic field with $\mathbf{b} = \mathbf{B}/B$, reduces to

$$\Gamma_i(\mathbf{R}_g, \mu, v_{\parallel}, t) = q_i \mathbf{A}_i^* \cdot \dot{\mathbf{R}}_g - \frac{\mu B}{\Omega_i} \dot{\theta} - m_i v_{\parallel}^2 / 2 - q_i \Phi_i, \quad (1)$$

with $q_i \Phi_i = q_i \phi + \mu B$ and $q_i \mathbf{A}_i^* = q_i \mathbf{A} + m_i v_{\parallel} \mathbf{b}$. We remark that, in Eq. (1), the electrostatic potential ϕ is evaluated at the gyrocenter position, i.e. $\phi = \phi(\mathbf{R}_g)$, such that ion FLR effects

are neglected. From Eq. (1), we deduce the ion equations of motion,

$$\dot{\mathbf{R}}_g = \mathbf{b} v_{\parallel} + \frac{\mathbf{E} \times \mathbf{b}}{B}, \quad (2a)$$

$$\dot{v}_{\parallel} = \frac{q_i}{m_i} \mathbf{b} \cdot \mathbf{E}, \quad (2b)$$

and $\dot{\mu} = 0$, with $v_{\parallel} = \dot{\mathbf{R}}_g \cdot \mathbf{b}$ and $\mathbf{E} = -\nabla \phi$ the electric field. Eq. (2a) describes the parallel streaming along the magnetic field lines and the perpendicular drift due to the $\mathbf{E} \times \mathbf{B}$ velocity, while Eq. (2b) represents the acceleration in the parallel direction associated with the electric field \mathbf{E} . Using the equations of motion given in Eq. (2), the evolution equation of the full-F (gyrophase-independent) ion distribution function, $F_i = F_i(\mathbf{R}_g, \mu, v_{\parallel}, t)$, in the electrostatic limit of the GK ion Boltzmann equation²⁰ is given by

$$\frac{\partial}{\partial t} (\mathcal{J}_i F_i) + \nabla \cdot (\mathcal{J}_i \dot{\mathbf{R}}_g F_i) + \frac{\partial}{\partial v_{\parallel}} (\mathcal{J}_i F_i \dot{v}_{\parallel}) = \mathcal{J}_i \mathcal{C}_i + \mathcal{J}_i S_i, \quad (3)$$

where $\mathcal{J}_i = B/m_i$ is the gyrocenter phase-space Jacobian, which is a constant in the case of linear devices. On the right-hand side of Eq. (3), $S_i = S_i(\mathbf{R}_g, \mu, v_{\parallel}) = S_{\mathcal{N}} + S_{\mathcal{E}}$ models the particle ($S_{\mathcal{N}}$) and energy ($S_{\mathcal{E}}$) sources and are defined by^{53,54}

$$S_{\mathcal{N}} = \mathcal{A}_{\mathcal{N}} F_{Mi}, \quad (4a)$$

$$S_{\mathcal{E}} = \mathcal{A}_{\mathcal{E}} \left(s_{\parallel i}^2 + x_i - \frac{3}{2} \right) F_{Mi}, \quad (4b)$$

respectively. We note that the sources, given in Eq. (4), neglect FLR and polarization effects associated with the transformation from particle to gyrocenter coordinate⁴⁸. In Eq. (4), the perpendicular normalized velocity-space coordinate is defined by $x_i = \mu B / T_{i0}$, while we use $s_{\parallel i} = (v_{\parallel} - U_{\parallel i}) / v_{Ti}$ (with $v_{Ti}^2 = 2T_{i0} / m_i$ and $U_{\parallel i} = \mathbf{b} \cdot \mathbf{u}_i = \int d\mathbf{v} F_i v_{\parallel} / N_i$ the ion parallel fluid velocity) for the normalized parallel velocity-space coordinate. Here, T_{i0} is the reference ion temperature, which is assumed constant in time and space. We remark that in previous fluid investigations of LAPD, the low ion temperature assumption ($T_i \ll T_e$) is used and the ion energy source is neglected.

The functions $\mathcal{A}_{\mathcal{N}} = \mathcal{A}_{\mathcal{N}}(x, y)$ and $\mathcal{A}_{\mathcal{E}} = \mathcal{A}_{\mathcal{E}}(x, y)$ in Eq. (4) are chosen to describe the spatial localization of the sources resulting from ionization processes due to fast electrons and ions⁵⁵. Neglecting the presence of localized sources (not uniform in z) near the end plates, we assume that these sources are a uniform in z and radially localized with a top-hat-like shape. For instance, $\mathcal{A}_{\mathcal{N}}(x, y)$ is given by²⁹

$$\mathcal{A}_{\mathcal{N}}(x, y) = \mathcal{A}_{\mathcal{N}0} 0.5 \left[1 - \tanh \left(\frac{r - r_s}{L_s} \right) \right] + \mathcal{A}_{\mathcal{N}\infty}, \quad (5)$$

where $r = \sqrt{x^2 + y^2}$ is the perpendicular distance from the center of the device ($r = 0$), r_s is the radial extent of the plasma source, $L_s > 0$ is its typical source decay scale length, \mathcal{A}_{N0} is a positive and constant coefficient, which represents the physical particle fuelling rate near the center of the device, while $\mathcal{A}_{N\infty}$ represents a small ($\mathcal{A}_{N\infty} \ll \mathcal{A}_{N0}$) positive and constant particle source away from $r \sim r_s$ added for numerical reasons, in particular, to avoid regions of small or negative plasma density. Similar definitions for $\mathcal{A}_{\mathcal{E}}(x, y)$, $\mathcal{A}_{\mathcal{E}0}$ and $\mathcal{A}_{\mathcal{E}\infty}$ are used. In Eq. (4), we also introduce a shifted Maxwellian distribution function defined by^{41,44}

$$F_{Mi} = \frac{N_i}{\pi^{3/2} v_{Ti}^3} e^{-s_{\parallel i}^2} e^{-x_i}, \quad (6)$$

which assumes isotropic ion temperatures. We remark that the sources given in Eq. (4) neglect non-Maxwellian sources, which can be relevant to fast ion injections, and that the functional form of Eq. (4) has a straightforward projection in the Hermite-Laguerre basis.

Finally, the term \mathcal{C}_i in Eq. (3) is a full-F and nonlinear collision operator model describing ion-ion collisions. In particular, we use a long-wavelength (neglecting FLR effects) Dougherty collision operator³⁹, given by

$$\mathcal{C}_i = v_i \frac{\partial}{\partial \mathbf{v}} \cdot \left[\frac{2T_i}{m_i} \frac{\partial}{\partial \mathbf{v}} F_i - (\mathbf{v} - \mathbf{u}_i) F_i \right], \quad (7)$$

where $T_i = \int d\mathbf{v} F_i m_i (\mathbf{v} - \mathbf{u}_i)^2 / (3N_i)$ and $\mathbf{u}_i = \int d\mathbf{v} F_i \mathbf{v} / N_i$ are the ion temperature and mean fluid velocity, and $v_i = 4\sqrt{\pi} N_i q_i^4 \ln \lambda / (3m_i^{1/2} T_{i0}^{3/2})$ is the ion-ion collision frequency, which is constant in the present work. The effects of ion-electron collisions are neglected in Eq. (3) since they occur on a time scale larger by, at least, a factor proportional to $\sqrt{m_i/m_e}$ than ion-ion collisions.

Eq. (3) is equivalent to the ion GK model used in previous GK turbulent simulations of LAPD, implemented in the Gkeyll³⁷ and in the GENE³⁸ codes. Both implementations use the same nonlinear Dougherty collision operator for ion-ion collisions (given in Eq. (7)) and neglect ion-electron collisions. The Gkeyll code employs a discontinuous-Galerkin approach and GENE uses a finite-volume method to discretize the velocity-space coordinates (v_{\parallel}, μ) , while our work uses the GM approach to simulate the full-F ion distribution function F_i . To our knowledge, this is the first time such a moment approach is applied to perform nonlinear full-F turbulent simulations with an arbitrary number of ion GMs.

B. Full-F ion GM Hierarchy Equation

Following Ref. 10, we perform the GM expansion of the full-F ion distribution function, F_i . More precisely, we expand F_i onto a set of Hermite, $H_p(s_{\parallel i})$, and Laguerre, $L_j(x_i)$, velocity-space polynomials⁵⁶, such that

$$F_i = \sum_{p=0}^{\infty} \sum_{j=0}^{\infty} \mathcal{N}^{pj} \frac{H_p(s_{\parallel i}) L_j(x_i)}{\sqrt{2^p p!}} \frac{F_{Mi}}{N_i}, \quad (8)$$

where \mathcal{N}^{pj} are the ion GMs, evaluated by using the Hermite and Laguerre orthogonality relations⁵⁶

$$\mathcal{N}^{pj} = 2\pi \int_{-\infty}^{\infty} dv_{\parallel} \int_0^{\infty} d\mu \frac{B}{m_i} F_i \frac{H_p(s_{\parallel i}) L_j(x_i)}{\sqrt{2^p p!}}. \quad (9)$$

By introducing the GM projector^{10,22,44,52}

$$\|\chi\|^{pj} = 2\pi \int_{-\infty}^{\infty} dv_{\parallel} \int_0^{\infty} d\mu \chi \frac{B}{m_i} F_i \frac{H_p(s_{\parallel i}) L_j(x_i)}{\sqrt{2^p p!}}, \quad (10)$$

with $\chi = \chi(\mathbf{R}_g, \mu, v_{\parallel}, t)$ being an arbitrary gyrocenter phase-space function, we find $\mathcal{N}^{pj} = \|\chi\|^{pj}$ from Eq. (10). We remark that, in Eq. (8), the shift of the parallel velocity coordinate $s_{\parallel i}$, appearing in F_{Mi} defined in Eq. (6) and in the argument of the Hermite polynomial H_p , is necessary to ensure good convergence property of the GM approach with respect to the number of GMs in Eq. (8), in particular in the presence of sonic ion flows (see Sec. IV C). These flows appear at the sheath entrance where ions are accelerated to the ion sound speed (see Sec. II G). Additionally, we note that F_{Mi} , defined in Eq. (6), is assumed to have the same parallel and perpendicular temperature, $T_{\parallel i} = T_{\perp i} = T_{i0}$. The assumption of an isotropic Maxwellian distribution in Eq. (8) is justified by the large ion-ion collision frequency typically found in a linear plasma device (where $T_i \lesssim 1$ eV) compared to the boundary region in fusion devices (where $T_i \gtrsim 10$ eV). The absence of strong external energy sources driving temperature anisotropy in LAPD experiments supports this assumption (see Eq. (4)).

The lowest-order GMs can be related to fluid ion gyrocenter quantities, such as the ion gyrocenter density N_i , the ion parallel velocity $U_{\parallel i}$, and the ion parallel and perpendicular pressure and temperature $P_{\parallel i} = T_{\parallel i} N_i$ and $P_{\perp i} = T_{\perp i} N_i$, respectively. Indeed, using Eq. (9), we derive that

$$N_i = \mathcal{N}^{00}, \quad (11a)$$

$$\mathcal{N}^{10} = 0, \quad (11b)$$

$$\begin{aligned} P_{\parallel i} &= N_i T_{\parallel i} = 2\pi \int_{-\infty}^{\infty} dv_{\parallel} \int_0^{\infty} d\mu B F_i (v_{\parallel} - U_{\parallel i})^2 \\ &= T_{i0} \left(\sqrt{2} \mathcal{N}^{20} + N_i \right), \end{aligned} \quad (11c)$$

$$\begin{aligned} P_{\perp i} &= N_i T_{\perp i} = 2\pi \int_{-\infty}^{\infty} dv_{\parallel} \int_0^{\infty} d\mu \frac{B}{m_i} \mu B F_i \\ &= T_{i0} (N_i - \mathcal{N}^{01}), \end{aligned} \quad (11d)$$

with the total ion temperature defined by $T_i = \int d\mathbf{v} F_i m_i (\mathbf{v} - \mathbf{u}_{\parallel i})^2 / (3N_i) = (T_{\parallel i} + 2T_{\perp i})/3 =$

$T_{i0}(\sqrt{2}\mathcal{N}^{20} + 3N_i - 2\mathcal{N}^{01})/(3N_i)$. We remark that Eq. (11b) is a direct consequence of our choice of using a shifted parallel velocity-space coordinate $s_{\parallel i}$ in Eq. (8). In Appendix A, we use the definitions of Eq. (11) to derive the Braginskii ion temperature equation. We note that the ion gyrocenter fluid quantities given in Eq. (11) are equivalent to the particle ones since FLR and polarization effects^{14,48,52}, associated with the transformation from particle to gyrocenter coordinates, are neglected in our model.

We now derive the full-F GM hierarchy equation describing the evolution of an arbitrary number of GMs, \mathcal{N}^{pj} . This is obtained by projecting the ion full-F equation given in Eq. (3) onto the Hermite-Laguerre basis. In addition, we normalize time t to R/c_{s0} (with $c_{s0} = \sqrt{T_{e0}/m_i}$ the ion sound speed evaluated at the reference constant electron temperature T_{e0} and R the radial extension of the plasma chamber in the direction perpendicular to \mathbf{B}), the potential ϕ to T_{e0}/e , the parallel and perpendicular spatial scales to R and $\rho_{s0} = c_{s0}/\Omega_i$, respectively. We also normalize the ion and electron densities, N_i and N_e , to the constant reference density N_0 , the parallel electron velocity $U_{\parallel e}$ to c_{s0} , and the electron temperature, T_e , to T_{e0} . In addition, we assume $q_i = +e$, considering a hydrogen plasma. Hence, we derive the normalized ion GM hierarchy equation, which describes the evolution of the GMs \mathcal{N}^{pj} , i.e.

$$\begin{aligned} & \frac{\partial}{\partial t} \mathcal{N}^{pj} + \sqrt{\frac{p}{\tau_i}} \mathcal{N}^{p-1j} \frac{\partial}{\partial t} U_{\parallel i} + \nabla \cdot \|\dot{\mathbf{R}}_g\|^{pj} \\ & + \sqrt{\frac{p}{\tau_i}} \|\dot{\mathbf{R}}_g\|^{p-1j} \cdot \nabla U_{\parallel i} - \sqrt{\frac{p}{\tau_i}} \|\dot{v}_{\parallel}\|^{p-1j} = \mathcal{C}_i^{pj} + S_{\mathcal{N}}^{pj} + S_{\mathcal{E}}^{pj}, \end{aligned} \quad (12)$$

where the GM projections are given by

$$\begin{aligned} \nabla \cdot \|\dot{\mathbf{R}}_g\|^{pj} &= \sqrt{\tau_i} \partial_z \left(\sqrt{p+1} \mathcal{N}^{p+1j} + \sqrt{p} \mathcal{N}^{p-1j} \right) \\ &+ \partial_z (U_{\parallel i} \mathcal{N}^{pj}) + \frac{1}{\rho_*} [\phi, \mathcal{N}^{pj}], \end{aligned} \quad (13a)$$

$$\begin{aligned} \sqrt{\frac{p}{\tau_i}} \|\dot{\mathbf{R}}_g\|^{p-1j} \cdot \nabla U_{\parallel i} &= \left(p \mathcal{N}^{pj} + \sqrt{p(p-1)} \mathcal{N}^{p-2j} \right. \\ &+ \left. \sqrt{\frac{p}{\tau_i}} U_{\parallel i} \mathcal{N}^{p-1j} \right) \partial_z U_{\parallel i} + \sqrt{\frac{p}{\tau_i}} \frac{1}{\rho_*} \mathcal{N}^{p-1j} [\phi, U_{\parallel i}], \end{aligned} \quad (13b)$$

$$\sqrt{\frac{p}{\tau_i}} \|\dot{v}_{\parallel}\|^{p-1j} = -\mathcal{N}^{p-1j} \sqrt{\frac{p}{\tau_i}} \partial_z \phi, \quad (13c)$$

with $\rho_* = \rho_{s0}/R$ and $\tau_i = T_{i0}/T_{e0}$. In Eq. (13), we introduce the Poisson bracket operator that is $[f, g] = \partial_x f \partial_y g - \partial_y f \partial_x g$. The GM expansions of the particle and energy sources, $S_{\mathcal{N}}^{pj}$ and $S_{\mathcal{E}}^{pj}$, are given by

$$S_{\mathcal{N}}^{pj} = \mathcal{A}_{\mathcal{N}} \delta_p^0 \delta_j^0 = S_{\mathcal{N}}, \quad (14a)$$

$$S_{\mathcal{E}}^{pj} = \mathcal{A}_{\mathcal{E}} \left(\frac{\delta_p^2 \delta_j^0}{\sqrt{2}} - \delta_p^0 \delta_j^1 \right), \quad (14b)$$

respectively. The contribution of Eq. (14a) to the ion density equation obtained with $(p, j) = (0, 0)$ represents particle sources, while the non-vanishing terms with $(p, j) = (2, 0)$ and $(0, 1)$ in Eq. (14b) are associated with parallel and perpendicular energy sources.

Finally, we express the nonlinear Dougherty collision operator in terms of GMs. We first express Eq. (7) in terms of the velocity-space coordinates $(s_{\parallel i}, x_i)$ and project it onto the Hermite-Laguerre basis. This yields

$$\begin{aligned} \mathcal{C}_i^{pj} &= v_i \left[-(p+2j) \mathcal{N}^{pj} + (T_i - 1) \right. \\ &\times \left. \left(\sqrt{p(p-1)} \mathcal{N}^{p-2j} - 2j \mathcal{N}^{pj-1} \right) \right], \end{aligned} \quad (15)$$

where T_i is expressed in terms of the GMs using Eq. (11). The nonlinear Dougherty collision operator conserves particles ($\mathcal{C}_i^{00} = 0$), momentum ($\mathcal{C}_i^{10} = 0$) and energy ($\mathcal{C}_i^{20} = \sqrt{2} \mathcal{C}_i^{01}$). While simpler in form compared to the GM expansion of the nonlinear Fokker-Planck Landau collision operator¹⁴, the Dougherty collision operator constitutes an initial step to incorporate advanced collisional effects in the nonlinear and full-F ion GM hierarchy equation. The numerical implementation of the nonlinear Fokker-Planck Landau collision operator¹⁴ will be considered in future work.

To obtain the time evolution of the GMs \mathcal{N}^{pj} , it is necessary to derive an explicit expression for the time derivative of the ion parallel velocity, $\partial_t U_{\parallel i}$ which appears in Eq. (12) and resulting from the use of the shifted parallel velocity-space coordinate $s_{\parallel i}$. By setting $(p, j) = (1, 0)$ in Eq. (12) and using the fact that \mathcal{N}^{10} vanishes exactly (see Eq. (11b)), we derive the desired expression for $\partial_t U_{\parallel i}$ given by

$$N_i \partial_t U_{\parallel i} + \frac{N_i}{\rho_*} [\phi, U_{\parallel i}] + \tau_i \partial_z P_{\parallel i} + N_i U_{\parallel i} \partial_z U_{\parallel i} + N_i \partial_z \phi = 0, \quad (16)$$

where the parallel ion pressure $P_{\parallel i}$ is expressed in terms of GMs according to Eq. (11c).

We note that the full-F GM hierarchy equation, given in Eq. (12), can also be derived from the electromagnetic full-F GM hierarchy equation described in Ref. 10. This is achieved by considering the electrostatic limit, neglecting FLR effects, and assuming isotropic and constant ion temperatures in F_{Mi} . We remark that, if F_{Mi} is normalized with the local parallel and perpendicular ion temperatures ($T_{\parallel i}$ and $T_{\perp i}$ in Eq. (11c) and Eq. (11d), respectively) as in Ref. 10, additional terms proportional to their time derivatives and gradients appear in Eq. (12). These terms might be important in the case of large temperature variations such as the ones in the boundary, but can be neglected in the case of LAPD.

Notably, the GMs with different p are coupled in Eq. (12) due to the parallel streaming terms, associated with the ion

Landau damping. On the other hand, the GMs with different j are only coupled through the collision operator (see Eq. (15)) as our model neglects FLR effects yielding additional coupling in j^{12} . As a result, a few Laguerre GMs are expected to be sufficient in our nonlinear turbulent simulations.

To carry out the numerical turbulent simulations presented here, a simple closure by truncation is applied to the GM hierarchy equation. More precisely, we set $\mathcal{N}^{pj} = 0$ for all $(p, j) > (P, J)$ with $0 \leq P, J < \infty$. The full-F GM hierarchy equation enables us to perform turbulent simulations of LAPD using an arbitrary number of GMs. Different values of (P, J) are considered in Sec. IV where we demonstrate that the closure by truncation is sufficient to perform full-F turbulent simulations in our case.

C. Cold-ion reduced model

We consider here the cold-ion limit of the full-F GM hierarchy and derive a simplified model, similar to the one used in previous turbulent investigations of linear devices based on fluid models (see, e.g., Refs. 29, 34, and 35) where the effects of finite ion temperature T_i are neglected.

In the cold ion limit ($T_i = 0$), only the GM \mathcal{N}_i^{00} and $U_{\parallel i}$, associated with the ion gyrocenter density and the parallel ion velocity, need to be evolved and the contribution from the parallel ion pressure $P_{\parallel i}$ in Eq. (16) can be neglected. As a consequence, the ion GM hierarchy equation given in Eq. (12) reduces to the ion gyrocenter continuity equation for N_i and to the ion parallel momentum equation for $U_{\parallel i}$ ^{47,48,57}, i.e.

$$\frac{\partial}{\partial t} N_i + \frac{1}{\rho_*} [\phi, N_i] + \partial_z (U_{\parallel i} N_i) = S_{\mathcal{N}}, \quad (17a)$$

$$\partial_t U_{\parallel i} + \frac{1}{\rho_*} [\phi, U_{\parallel i}] + U_{\parallel i} \partial_z U_{\parallel i} + \partial_z \phi = 0, \quad (17b)$$

respectively. We remark that the particle and momentum conservation of the collision operator is used in deriving Eq. (17).

D. Electron fluid model

We use the Braginskii model to evolve the electron dynamics, avoiding the evolution of their distribution function, in contrast to Refs. 37 and 38. The fluid approach for the electrons is justified when the electron collision frequency is much larger than the ion collision frequency and electron FLR effects are negligible for modes developing at $k_{\perp} \rho_s \sim 1$, which is the case of LAPD experiments. In the absence of electron FLR effects, the electron particle and gyrocenter position coincide such that no distinction is made between the electron particle and gyrocenter fluid quantities. Hence, the time evolution of the electron density n_e , electron parallel velocity $U_{\parallel e}$, and temperature T_e is determined by the continuity equation, the generalized Ohm's law, and the temperature equation, respectively. These equations are given by

$$\partial_t n_e + \frac{1}{\rho_*} [\phi, n_e] + \partial_z (U_{\parallel e} n_e) = S_{\mathcal{N}}, \quad (18a)$$

$$\begin{aligned} \partial_t U_{\parallel e} + \frac{1}{\rho_*} [\phi, U_{\parallel e}] + U_{\parallel e} \partial_z U_{\parallel e} = & \frac{m_i}{m_e} [v_{\parallel} J_{\parallel} + \partial_z \phi \\ & - \frac{T_e}{n_e} \partial_z n_e - 1.71 \partial_z T_e], \end{aligned} \quad (18b)$$

$$\begin{aligned} \partial_t T_e + \frac{1}{\rho_*} [\phi, T_e] + U_{\parallel e} \partial_z T_e = & \frac{2}{3} T_e \left(\frac{0.71}{N_e} \partial_z J_{\parallel} - \partial_z U_{\parallel e} \right) \\ & + \partial_z (\chi_{\parallel e} \partial_z T_e) + S_{T_e}, \end{aligned} \quad (18c)$$

where the normalized parallel electrical resistivity and electron thermal conductivity are given by $v_{\parallel} = v_0 / T_e^{3/2}$ and $\chi_{\parallel e} = 1.075 T_e^{5/2} / v_0$, respectively. Here, $v_0 = 4\sqrt{2\pi} e^4 n_{e0} R \sqrt{m_e} \ln \lambda / [3c_{s0} m_i T_{e0}^{3/2} 1.96]$ is the normalized electron collisionality. On the right-hand side of Eq. (18a) and Eq. (18c), $S_{\mathcal{N}}$ and S_{T_e} are the normalized density and temperature sources. In Eq. (18), the parallel electrical current is $J_{\parallel} = n_e (U_{\parallel i} - U_{\parallel e})$.

E. Vorticity equation

We now obtain the vorticity equation that governs the evolution of the electrostatic potential ϕ . This equation imposes the charge conservation constraint to the time evolution of the plasma densities and electrical currents.

To derive the vorticity equation, we consider the quasineutrality condition in the long-wavelength limit, given by^{10,20}

$$-en_e + q_i N_i = -\nabla \cdot \left(\frac{q_i^2 N_i}{m_i \Omega_i^2} \nabla_{\perp} \phi \right). \quad (19)$$

We remark that Eq. (19) neglects FLR effects (associated with the gyro-average) but retains the polarization effect in its right-hand side. Including high-order FLR contributions to the gyro-average and polarization terms, which are important for predicting of small-scale fluctuations⁵¹, requires the development of FLR closures at arbitrary wavelength (see, e.g., Ref. 50) using an arbitrary number of GMs, a task left to future work. We also notice that Eq. (19) is equivalent to the quasineutrality condition used in previous GK turbulent simulations of LAPD^{37,38} if the Boussinesq approximation is used, i.e. if N_i is approximated by N_0 on the right-hand side of Eq. (19). The Boussinesq approximation is widely used in fluid codes^{8,36} and is also considered below to derive the vorticity equation.

While Eq. (19) can be solved to obtain ϕ given the electron and ion densities, n_e and N_i respectively, we use a vorticity equation instead which is often considered in turbulent fluid codes^{29,34-36}. The vorticity equation is derived by taking the time derivative of the quasineutrality equation given

in Eq. (19) and by using the electron and ion continuity equations, given in Eqs. (17a) and (18a), respectively. Furthermore, we use the Boussinesq approximation, such that

$$\nabla \cdot \left(\frac{q_i^2 N_i}{m_i \Omega_i^2} \nabla_{\perp} \phi \right) \simeq \frac{q_i^2 N_i}{m_i \Omega_i^2} \Omega, \quad (20)$$

where we introduce the vorticity variable $\Omega = \nabla_{\perp}^2 \phi$. The vorticity equation is then

$$-\partial_t \Omega - \frac{1}{\rho^*} [\phi, \Omega] - \partial_z (U_{\parallel i} \Omega) + \frac{1}{N_i} \partial_z J_{\parallel} = 0, \quad (21)$$

We note that the effects of the Boussinesq approximation on plasma turbulence are the subject of previous studies^{36,51,58-60}. While it might not be justified in LAPD when steep density gradients are present, it allows us to reduce the computational cost of our simulations when inverting the two-dimensional Laplacian to obtain ϕ from the vorticity variable Ω . We use the vorticity equation given in Eq. (21) to evolve Ω when considering the full-F ion GM hierarchy equation and the cold ion models, given in Eqs. (12) and (17) respectively, coupled to the fluid electron model in Eq. (18).

F. Two-fluid Braginskii fluid model

We finally introduce the two-fluid Braginskii fluid model⁹, valid in the high-collisional regime, for comparison with the full-F ion GM hierarchy equation and the cold-ion model.

We first note that, in the two-fluid Braginskii model, quasineutrality is assumed (neglecting the polarization term in Eq. (19)) and, as a consequence, the electron particle density is used as an independent variable, such that $n_e \simeq N_i$. On the other hand, ion polarization effects are retained by the presence of the polarization drift (neglected in Eq. (2a)) in the ion particle continuity equation, from which the vorticity equation (given below) is derived for the electrostatic potential. Furthermore, since FLR effects associated with the difference between particle and gyrocenter positions are neglected in the two-fluid Braginskii fluid model, the ion gyrocenter fluid quantities, such as ion parallel velocity $U_{\parallel i}$ and ion temperature T_i , are assumed to be equal to particle fluid quantities.

In addition to the fluid electron fluid equations for n_e , $U_{\parallel e}$ and T_e already described in Sec. IID, the two-fluid Braginskii equations prescribe a parallel ion momentum equation to evolve $U_{\parallel i}$, an ion temperature equation to evolve T_i , and vorticity equations for Ω . These equations are given by

$$\begin{aligned} \partial_t U_{\parallel i} + \frac{1}{\rho^*} [\phi, U_{\parallel i}] + U_{\parallel i} \partial_z U_{\parallel i} = & -\partial_z T_e - \tau_i \partial_z T_i \\ & - (T_e + \tau_i T_i) \frac{\partial_z n_e}{n_e}, \end{aligned} \quad (22a)$$

$$\begin{aligned} \partial_t T_i + \frac{1}{\rho^*} [\phi, T_i] + U_{\parallel i} \partial_z T_i = & + \frac{2}{3} T_i \left[(U_{\parallel i} - U_{\parallel e}) \frac{\partial_z n_e}{n_e} - \partial_z U_{\parallel e} \right] \\ & + \partial_z (\chi_{\parallel i} \partial_z T_i) + \frac{\mathcal{A}_{\mathcal{E}}}{n_e} + (1 - T_i) \frac{\mathcal{A}_{\mathcal{N}}}{n_e}, \end{aligned} \quad (22b)$$

$$\begin{aligned} \partial_t \Omega + \tau_i \partial_t \nabla_{\perp}^2 T_i = & \frac{1}{n_e} \partial_z J_{\parallel} - \frac{1}{\rho^*} [\phi, \Omega + \tau_i \nabla_{\perp}^2 T_i] \\ & - U_{\parallel i} \partial_z (\Omega + \tau_i \nabla_{\perp}^2 T_i). \end{aligned} \quad (22c)$$

respectively. In Eq. (22b), $\chi_{\parallel i} = 1.32 \sqrt{m_e/m_i} (\tau_i T_i)^{5/2} / v_0$ is the normalized parallel ion thermal conductivity. In Eq. (22b), the two last terms are the ion temperature sources associated with the energy source $S_{\mathcal{E}}$ (see Eq. (14b)), which appears on the right-hand side of Eq. (3). In Appendix A, we demonstrate analytically how these terms are determined by deriving the ion temperature equation, Eq. (22b), from the ion GM hierarchy equation.

In contrast to the cold-ion model given in Eq. (17), the parallel electric field $\partial_z \phi$, appearing in the parallel ion momentum equation, Eq. (17b), is approximated in Eq. (22a) by the electron parallel pressure gradient, such that $\partial_z \phi \simeq \partial_z P_e$ with $P_e = n_e T_e$ (see Eq. (18b)). We also note that the terms proportional to the Laplacian of the ion temperature, i.e. $\tau_i \nabla_{\perp}^2 T_i$, present in the vorticity equation, Eq. (22c), are absent in Eq. (21), which is derived from the GM hierarchy equation. Indeed, these terms are associated with the long-wavelength FLR effect correction, which are neglected in Eq. (21) as FLR effects are omitted. While the ion temperature in LAPD experiments is generally lower than the electron temperature, it has been shown that FLR effects can be important in this regime. Further investigations are hence required to investigate the effects of finite ion temperature and related FLR effects on small scale fluctuations in LAPD.

G. Boundary conditions

Boundary conditions are required for the ion GMs, \mathcal{N}^{pj} , the electron fluid quantities, N_e , $U_{\parallel e}$, T_e , and the potential ϕ in the perpendicular (x, y) plane at $x = \pm L_x/2$ and $y = \pm L_y/2$ and at the end plates located in the z direction at $z = \pm L_z/2$, where a sheath forms due to the plasma-wall interaction.

At $x = \pm L_x/2$ and $y = \pm L_y/2$, homogenous Neumann boundary conditions are used for all quantities. These *ad-hoc* boundary conditions have a negligible effect on plasma turbulence near the center of the device as they are imposed at a distance sufficiently large from the center of the device. On the other hand, the boundary conditions in the z direction have an important impact since the formation of a Debye sheath is observed when the magnetic field lines intercept the end plates that control the plasma losses⁶¹. Since the sheath region cannot be modeled by the field equations derived in Sec. II E (the GK formalism is violated in this region), the sheath is modeled in our simulations by a set of appropriate boundary conditions imposed at the sheath entrance.

In previous GK simulations of LAPD^{37,38}, a conducting wall is considered. Accordingly, the fraction of electrons that cross the sheath and are lost being absorbed by the walls is determined by the value of the potential at the sheath entrance. This fraction is imposed by evaluating the cutoff velocity of the electron distribution function numerically. Leveraging the GM approach, we use the standard fluid Bohm boundary conditions⁶¹ which sets the value of the parallel electron and ion velocities, $U_{\parallel e}$ and $U_{\parallel i}$, at the sheath entrance. Therefore, we assume that^{31,62}

$$U_{\parallel e}(x, y, z = \pm L_z/2) = \pm \sqrt{T_{e,s}} e^{\Lambda - \phi_s/T_{e,s}}, \quad (23a)$$

$$U_{\parallel i}(x, y, z = \pm L_z/2) = \pm c_s \\ = \pm \sqrt{T_{e,s}} \sqrt{1 + \tau_i T_{i,s}/T_{e,s}}, \quad (23b)$$

with $\Lambda = \log m_i/(2m_e) \simeq 3$ for hydrogen plasmas. In Eq. (23), $T_{e,s}$ and $T_{i,s}$ are the electron and ion temperatures evaluated at the sheath entrance, i.e. $T_{e,s} = T_e(x, y, z = \pm L_z/2)$ and $T_{i,s} = T_i(x, y, z = \pm L_z/2)$, and, similarly $\phi_s = \phi(x, y, z = \pm L_z/2)$. We notice that the boundary conditions in Eq. (23) reduce to the ones used in Ref. 29 when $T_i \ll T_e$ and correspond to the ones used in SOL turbulent simulations using the drift-reduced Braginskii model⁸. For the remaining quantities, we assume, for simplicity, that the gradients of electron density, n_e , electron temperature, T_e , ion GMs, \mathcal{N}^{pj} , and electrostatic potentials, ϕ , vanish along the direction of the magnetic field at the sheath entrance, i.e. homogenous Neumann boundary conditions are imposed at $z = \pm L_z/2$. While the homogenous Neumann boundary conditions considered here are sufficient to ensure the numerical stability of the present simulations, further investigations are needed to develop first-principles sheath boundary conditions for the GM approach. In particular, the analytical procedure outlined in, e.g., Refs. 31 and 62, can be extended to an arbitrary number of GMs and kinetic sheath boundary conditions can also be developed^{63–65}. Magnetic field lines intercept the machine wall with a small oblique angle in fusion devices, further complicating the treatment of the sheath boundary conditions^{30,32}.

III. NUMERICAL IMPLEMENTATION

To solve the full-F ion GM hierarchy given in Eq. (12) coupled with the electron fluid model in Eq. (18) and the vorticity equation in Eq. (21), we have developed a new three-dimensional full-F simulation code. This code solves the turbulent dynamics for an arbitrary number of ion GMs. It also solves the cold ion model (Sec. II C) and the two-fluid Braginskii model (Sec. II F) for comparison with the GM results.

To evolve the plasma dynamics, we employ similar numerical algorithms as the two-fluid GBS code⁸. More precisely, an explicit fourth-order Runge-Kutta time-stepping scheme is used. The perpendicular and parallel directions are discretized using a uniform cartesian grid in the (x, y, z) coordinates with the x , y , and z directions discretized using N_x , N_y and N_z points

uniformly distributed between the intervals $[-L_x/2, +L_x/2]$, $[-L_y/2, +L_y/2]$ and $[-L_z/2, L_z/2]$, respectively. The Poisson bracket operator, $[f, g] = \mathbf{b} \times \nabla f \cdot \nabla g = \partial_x f \partial_y g - \partial_y f \partial_x g$, with $\mathbf{b} = \mathbf{B}/B = \mathbf{e}_z$, is evaluated by using a fourth-order Arakawa method⁶⁶. The numerical evaluation of the other spatial operators appearing in the GM hierarchy equation is based on a fourth-order and centered finite difference scheme, resulting in a 5-points centered stencil⁸. To avoid checkerboard patterns⁶⁰, the grid used to evolve the parallel velocities, $U_{\parallel e}$ and $U_{\parallel i}$, and the GMs \mathcal{N}^{pj} with odd p , is staggered to the left along the z -direction by $\Delta z/2$ (Δz is the grid spacing) with respect to the grid where the other fluid quantities, i.e. n_e , T_e , Ω (and thus ϕ), and the GMs \mathcal{N}^{pj} with even p are evaluated. Fourth-order interpolation techniques are used between two staggered grids⁶⁰. To improve the numerical stability of our numerical simulations, parallel and perpendicular numerical diffusions, such as

$$D(f) = \eta_{\perp} (\partial_{xx}^2 + \partial_{yy}^2) f + \eta_z \partial_{zz}^2 f, \quad (24)$$

where f denotes one of the evolved quantities, are added to the right-hand side of all equations. We choose the perpendicular and parallel diffusion coefficients, η_{\perp} and η_z , to be constant and sufficiently small not to affect significantly the results. The model is implemented in a Fortran code using a MPI domain decomposition in all spatial directions. As a consequence, the computation cost of our simulations scales approximately linearly with the number of GMs taken into account.

The initial conditions of the turbulent nonlinear simulations impose equal electron and ion densities and temperatures, such that $n_e = \mathcal{N}^{00}$ and $T_e = T_i$ with top-hat-like profiles in the perpendicular plane and uniform in z , similar to Eq. (5), such that $f = \mathcal{A}_0 [1 - \tanh\{(r - r_s)/(4L_s)\}]/2$. We use $\mathcal{A}_0 = 0.4$ for $f = n_e$ and $\mathcal{A}_0 = 0.4$ for $f = T_e$. In addition, we set $\phi = \Lambda T_e$ to avoid unphysical and large electron current into the sheath region. The initial values of \mathcal{N}^{20} and \mathcal{N}^{01} , given the initial ion density \mathcal{N} and ion temperature T_i profiles, are obtained by inverting Eq. (11), which yields $\mathcal{N}^{20} = N_i(T_i - 1)/\sqrt{2}$ and $\mathcal{N}^{01} = N_i(1 - T_i)$, with $T_{\parallel i} = T_{\perp i} = T_i$. Finally, the parallel velocities, $U_{\parallel i}$ and $U_{\parallel e}$, are initialized with smooth profiles along z , interpolating the values at the end plates fixed according to the boundary conditions given in Eq. (23). Random noise (with constant amplitude 0.01) is added to the initial densities, n_e and N_i , temperatures T_i (and associated GMs \mathcal{N}^{01} , \mathcal{N}^{02}), and parallel velocities, $U_{\parallel e}$ and $U_{\parallel i}$, profiles to seed turbulence. Typically, a quasi-steady state is achieved after $100 c_{s0}/R$ time unit (corresponding to $t \sim 4$ ms), where the sources of particle and energy are compensated by the losses at the end plates.

IV. FULL-F TURBULENT SIMULATION RESULTS

In this section, we present the first turbulent and full-F simulations of the GM approach of a linear plasma device, focusing on the parameters of the LAPD experiment. We perform

a comparison between the turbulent predictions of the full-F GM approach (see Sec. II B), with different numbers of GMs and values of collisionality and compare them with the Braginskii model introduced in Sec. II F.

Our simulations parameters are similar to those used in Ref. 29, where a helium LAPD plasma is considered. These parameters are summarized as follows: $n_{e0} = 2 \times 10^{12} \text{ cm}^{-3}$, $T_{e0} = 6 \text{ eV}$, $T_{i0} = 3 \text{ eV}$ ($\tau_i = 0.5$), $\Omega_i \sim 960 \text{ kHz}$, $\rho_{s0} = 1.4 \text{ cm}$, $c_{s0} = 1.3 \times 10^6 \text{ cm s}^{-1}$, $m_i/m_e = 400$ and $v_0 = 0.03$. The LAPD vacuum chamber has a radius $R \simeq 0.56 \text{ m}$ (i.e., $R \simeq 40\rho_{s0}$) and a parallel length of $L_z \simeq 18 \text{ m}$, such that we use $L_x = L_y = 100\rho_{s0}$ (or $L_x \sim L_y \sim 1.4 \text{ m}$) and $L_z = 36R$. The reference time is $R/c_{s0} \sim 43 \mu\text{s}$. We consider the following parameters for the density and temperature sources $L_s = 1\rho_{s0}$, $r_s = 20\rho_{s0}$, $\mathcal{A}_{\mathcal{N}0} = \mathcal{A}_{T_0} = 0.04$ (with $\mathcal{A}_{\mathcal{N}\infty} = \mathcal{A}_{T\infty} = 0.001$) and $\mathcal{A}_{\mathcal{E}0} = 0.02$ (with $\mathcal{A}_{\mathcal{E}\infty} = \mathcal{A}_{\mathcal{N}\infty}$). We use a numerical resolution of $N_x = N_y = 192$ in the perpendicular plane, which corresponds to a grid spacing of $\sim 0.52\rho_{s0}$. This resolution is also sufficient to resolve turbulence occurring at perpendicular wavelengths longer than ρ_{s0} in the perpendicular plane, which is dominated by the long-wavelength KH instability²⁹. On the other hand, a coarser resolution of $N_z = 64$ is used in the parallel direction. Given our numerical resolution, we use $\eta_{\perp} = 0.05$ and $\eta_z = 5$ for numerical stability. We remark that further numerical studies are required to fully assess the impact of the numerical diffusion and resolution we use in our simulations, but the values considered here are sufficient for the goals of the present work.

In order to investigate the impact of ion collisions, we conduct a set of nonlinear simulations in the high (HC) and low (LC) ion collisionality regime. For each set, we consider different numbers of GMs (P, J) to investigate the convergence of the GM approach. More precisely, we consider $(P, J) = (2, 1)$, $(6, 1)$, and $(12, 1)$ in the LC regime and $(P, J) = (2, 1)$ and $(6, 1)$ in the HC regime. We change the ion collisionality by varying the ion collision frequency ν_i as an independent parameter while keeping all other parameters constant. In the HC regime, the ion collision frequency is computed using the LAPD physical parameters, such that $\nu_i = 1.38 \sqrt{m_i/m_e} v_0 / \tau_i^{3/2} \simeq 2.34$. In this regime, the ion mean-free-path, λ_{mpf} , is considerably shorter than the total length L_z , i.e. $\lambda_{mpf}/L_z \simeq \sqrt{2}\tau_i R/L_z/\nu_i \ll 1$, and the effects of the collision operator are expected to be important. On the other hand, we set the ion collision frequency to be small in the LC regime, such that $\nu_i \simeq 4 \times 10^{-3}$ yielding $\lambda_{mpf}/L_z \sim 6.9$. In this regime, the effect of the collision operator on the GMs is expected to be negligible. In all cases, no artificial diffusion in velocity-space is added, since the damping of the GMs by the Dougherty collision operator given in Eq. (15) is sufficient to ensure stability of our simulations.

We remark that using $J = 1$ is expected to be sufficient to represent the ion distribution function F_i in x_i since kinetic effects such as magnetic drifts¹² and trapped particles¹³ (which couple GMs with different j) are absent in the LAPD configuration. In addition, neglecting the gyro-average in our ion model allows us to remove the coupling between different j driven by the x_i -dependence of the gyro-average operator¹⁰. We also note that a number $J = 1$ of Laguerre polynomials

fully resolves the density and energy sources (see Eq. (14)). As a matter of fact, the only coupling to the $j \geq 2$ GMs is from the pitch-angle scattering contained in the collision operator given in Eq. (15), which is dominated by collisional damping. Indeed, if collisions are neglected GMs with $j > 1$ are completely decoupled from the the GMs with $j \leq 1$

This section is structured as follows. First, Sec. IV A provides an analysis and comparison of simulations based on the full-F GM hierarchy, the cold-ion, and the Braginskii models. Second, the turbulence characteristics are analyzed and compared in more details in Sec. IV B. Finally, we investigate the ion distribution function in velocity-space in Sec. IV C and the GM spectrum in quasi-steady state in Sec. IV D as a function of the number of GMs and for the two collisionality regimes.

A. Simulation results

This section presents a set of nonlinear and turbulent simulations of the LAPD using the full-F GM hierarchy equation given in Eq. (12), the cold-ion model in Eq. (17), and the Braginskii model introduced in Eq. (22).

A typical nonlinear evolution of the electron density, n_e , obtained by using the GM hierarchy equation with $(P, J) = (6, 1)$ GMs in the HC regime is shown in Fig. 1. For $t \lesssim 21R/c_{s0}$, the profiles build up because of the localized particle and energy sources present in the system. The steep density and temperature gradients near $r \sim r_s$ drive an unstable resistive drift-wave (not visible in Fig. 1 due to their small relative amplitude), with the most unstable mode occurring at $k_{\perp}\rho_{s0} \sim 0.5$ (k_{\perp} is the perpendicular wavenumber) with finite parallel wavenumber and rotating in the ion diamagnetic direction. Large poloidal flows, with velocity typically larger than the phase-velocity of the resistive drift waves³⁴, nonlinearly trigger a KH instability, characterized by a long perpendicular wavelength ($k_{\perp}\rho_{s0} \ll 1$) and $k_{\parallel} \simeq 0$. The KH instability becomes clearly visible around $t \simeq 45R/c_{s0}$. This instability, which has been shown to dominate the radial transport in LAPD²⁹, saturates at $t \simeq 53R/c_{s0}$, transporting the plasma to the $r \gtrsim r_s$ region and yielding the broadening of the initial profiles. The role of the KH-dominated transport in our simulations is confirmed by the strong steepening of the profiles (similar to Ref. 29) when the nonlinear term $[\phi, \Omega]$ in Eq. (21) is artificially suppressed.

After $t \sim 130R/c_{s0}$ (similarly to previous GK and Braginskii turbulent simulations of LAPD^{34,38}), a quasi-steady state is reached. At this point when the sources are compensated by the losses at the end plates. In particular, the quasi-steady state in our simulations can be monitored by examining the radial profiles. This is shown in Fig. 2, where the initial radial profile of n_e (associated with Fig. 1) reaches a quasi-steady state after $t \sim 130R/c_{s0}$. To support the steady-state assumption in our simulations, we present the time-averaged radial density profiles obtained over two time windows along with their associated standard deviations. As observed, the time-averaged density profiles remain the same (within their standard deviations). A similar qualitative evolution is observed with a higher number of GMs in the LC and HC regime, as

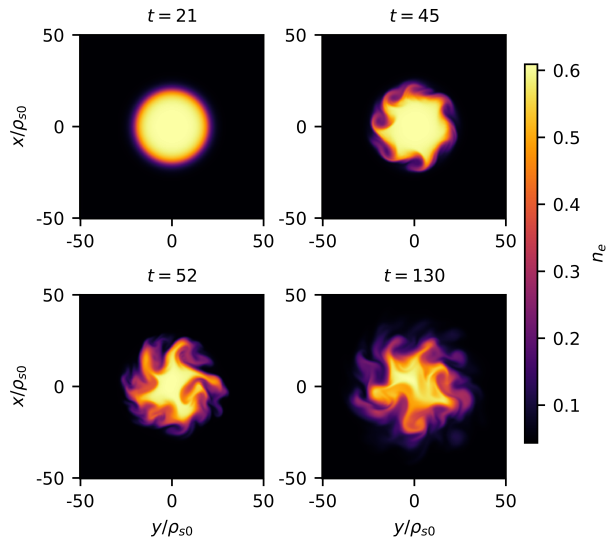


FIG. 1. Typical snapshots during the time evolution (from top-left to bottom-right) of a LAPD simulation using $(P, J) = (6, 1)$ GMs in the HC regime. The normalized electron density n_e (taken at $z = 0R$) is shown. First, the top-hat-like sources fuel the central region ($r \gtrsim r_s$) while a resistive drift-wave instability is triggered as the gradients build up (top left). Second, the KH instability develops (top right), saturates nonlinearly (bottom left), and broadens the profiles to reach a quasi-steady state (bottom right). n_e is normalized, as well as all the quantities shown in the following figures.

well as in the cold-ion and Braginskii simulations.

Regarding the computational cost, we remark that reaching a quasi-steady state requires a total of ~ 41500 CPU hours on the multi-core partition of the Piz Daint supercomputer, approximatively.

The dynamics in the direction parallel to the magnetic field is shown in Fig. 3 during the quasi-steady state. Instantaneous snapshots of the parallel turbulent structures of the electrostatic potential ϕ , electron density n_e , and electron temperature T_e reveal elongated structures. All quantities show weak parallel gradients $k_{\parallel} \simeq 0$, but have slightly larger values at the center ($z = 0$) and decrease in amplitude slowly near the end plates (located at $z = -18R$ and at $z = 18R$) due to the particle and energy losses caused by the sheath boundary conditions. Similar parallel structures are obtained when using a larger number of GMs. The turbulent structures observed in Fig. 3 are in qualitative agreement with previous fluid^{29,34,35} and GK^{37,38} turbulent simulations of LAPD.

We now examine the time-averaged radial profiles. These profiles are obtained by averaging over a time window of ~ 2 ms during the quasi-steady state as well as over the central region of LAPD, i.e. $-8R \leq z \leq +8R$ (or $-4\text{m} \lesssim z \lesssim 4\text{m}$), a region commonly considered to present experimental data⁴⁰ (a similar approach is used in previous GK simulations^{37,38}). More precisely, the averaged profile of the electrostatic potential ϕ is computed by defining $\langle \phi \rangle_{t,z} = \int_{-\ell_z/2}^{+\ell_z/2} dz \int_0^{\tau} dt \phi / (\ell_z \tau)$,

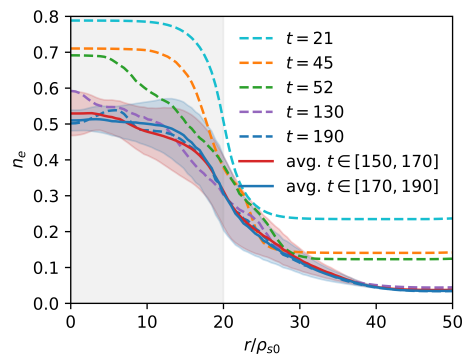


FIG. 2. Saturation of the radial profile of n_e (binned by radius) associated with Fig. 1 at $z = 0R$. Instantaneous radial profiles are shown by the dashed lines for different times, and time-averaged radial profiles over the time-windows $t \in [150, 170]$ (red) and $t \in [170, 190]$ (blue) are also presented for comparison. The shaded colored areas represent the standard deviations of each time-averaged profile. A quasi-steady state is reached for $t \gtrsim 130$. The time t is normalized to R/c_{s0} .

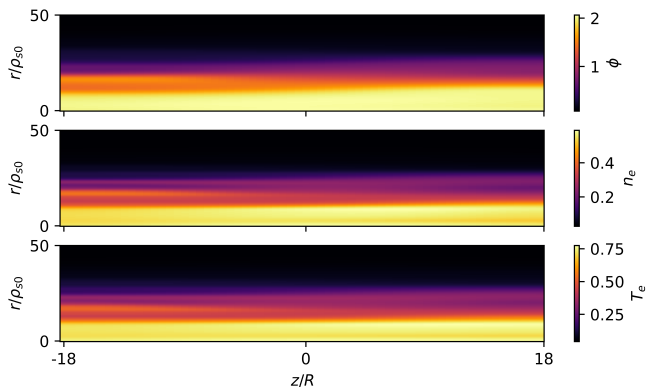


FIG. 3. Typical snapshots of the parallel turbulent structures of the electrostatic potential ϕ (top), electron density n_e (middle), and electron temperature T_e (bottom) using $(P, J) = (6, 1)$ GMs in the HC regime during the quasi-steady state and as a function of r . We notice that $\phi \sim 3T_e$.

with ℓ_z and τ are the z and time length of the average windows, respectively. The results are shown in Fig. 4, which displays the profiles of $\langle \phi \rangle_{t,z}$, $\langle n_e \rangle_{t,z}$, and $\langle T_e \rangle_{t,z}$ obtained in the GM simulations, using different numbers of GMs, in the cold-ion and the Braginskii simulations and as a function of the radius. Instantaneous profiles are also included for comparison.

We note, first, that the plasma profiles extend beyond r_s illustrating the broadening caused by the KH instability²⁹. More precisely, the profiles are approximatively constant close to the center of the device ($r < r_s$) and far from the source region ($r > r_s$), showing a region of steep gradients near $r \sim r_s$, where the fluctuation level is large (see Sec. IV B). Second, the time-averaged radial profiles from the GM simulations are very similar to the ones obtained from the Braginskii model. Third, no noticeable differences are found between the simulations in the LC and HC regimes and with dif-

ferent numbers of GMs. This suggests that ion kinetic effects may not significantly influence the predictions of the equilibrium (time-averaged) profiles in LAPD. On the other hand, the cold-ion model consistently predicts larger time-averaged radial profiles, while the gradients (not shown here) are of the same order as those obtained in the GM and Braginskii simulations. This difference between the cold-ion model and others cases with finite ion temperature is a consequence of the boundary conditions given in Eq. (23), as discussed below. Fourth, the analysis of the instantaneous profiles (indicated by dotted lines in Fig. 4) shows the existence of large perpendicular turbulent structures associated with the KH instability. Finally, we note that the time-averaged profiles obtained in Fig. 4 feature a similar behaviour of those obtained in previous fluid simulations²⁹ and GK simulations^{37,38}.

We remark that the electrostatic potential profile ϕ follows approximately the electron temperature T_e , as shown in Fig. 4. Indeed, $\phi \sim \Lambda T_e$ is required to have comparable electron and ion outflows in steady-state, such that $U_{\parallel i} \sim U_{\parallel e}$ near the end plates, according to Eq. (23). To verify that $\phi \sim \Lambda T_e$ in our simulations, we evaluate the radial profile of the instantaneous difference, $\phi - \Lambda T_e$, taken at the center of the device ($z = 0R$) for the GM (both the LC and HC regimes are considered), cold-ion and Braginskii simulations during the quasi-steady state. The results are shown in Fig. 5. We first observe that the GM and Braginskii simulations yield similar negative $\phi - \Lambda T_e$ values. On the other hand, $\phi - \Lambda T_e$ is roughly constant and approximately vanishes for all radii in the cold-ion model. The deviations observed in $\phi - \Lambda T_e$ are the result of the boundary conditions specified in Eq. (23). In fact, to achieve an equilibrium between parallel ion and electron flows, it is necessary that $\phi - \Lambda T_e \simeq -T_{e,s} \ln(1 + \tau_i T_{i,s}/T_{e,s})/2$ (as indicated by the black dotted line in Fig. 5) when finite ion temperature is considered in the case of Braginskii and GM simulations. In contrast, this condition reduces to $\phi - \Lambda T_e \simeq 0$ in the cold-ion model. Consequently, due to the finite ion temperature dependence of the boundary condition Eq. (23b), the equilibrium electrostatic potential ϕ exhibits higher amplitude in the cold ion model, which is confirmed in the time-averaged profiles observed in Eq. (4). Finally, in all cases considered, $\phi - \Lambda T_e$ remains smaller than the values of ϕ and ΛT_e ($\phi - \Lambda T_e \sim 0.1$ for $r \lesssim r_s$ compared to $\phi \sim \Lambda T_e \sim 2$, see Fig. 3).

B. Turbulence analysis

We now delve into the analysis of the turbulence properties, comparing the GM predictions with the Braginskii simulations. The instantaneous fluctuations are obtained by subtracting the time-averaged profiles from the full quantities, such that the fluctuation of, e.g., the electrostatic potential, $\tilde{\phi}$, is defined by $\tilde{\phi} = \phi - \langle \phi \rangle_t$, where $\langle \phi \rangle_t = \int_0^\tau dt \phi / \tau$ denotes the time-averaged potential. Similar definitions for the other quantities are used. The top panels of Fig. 6 show instantaneous snapshots of ϕ in the plane perpendicular at the center of the device $z = 0R$, while the bottom panels illustrate $\tilde{\phi}$ snapshots. The Braginskii, cold-ion, and GM simulations

with various (P, J) are considered.

We first observe that the fluctuations in the Braginskii model exhibits similar structures than those obtained in Ref. 35. In particular, the level of fluctuations is low at the center of the device and far from the source region, while it is large where the equilibrium gradient is steeper, in particular near $r \sim r_s$ (see Fig. 9). Notably, the $\tilde{\phi}$ snapshots reveal the presence of large amplitude structures propagating outwards. These observations hold for all the GM simulations, demonstrating qualitative agreement between the GM approach and the Braginskii model. While the fluctuations of the potential ϕ is not significantly affected by the number of GMs used in the simulation or by the collisionality regime, pointing out the fact that the KH instability (which drives turbulence) has a fluid nature, minor differences in the turbulent properties can still be observed. In fact, the use of a small number of GMs tends to produce slightly larger turbulent structures. This can be observed, for instance, by comparing the results of $(P, J) = (2, 1)$ with the $(12, 1)$ simulations in the LC regime. Finally, we observe that the cold-ion model produces the largest turbulent structures, which is consistent with the broad time-averaged profiles observed in Fig. 4. The same observations apply to the snapshots of the electron density n_e and its associated fluctuations \tilde{n}_e , as shown in Fig. 7. Similar plots are obtained for T_i and T_e , but not shown. Finally, it is worth noting that the fluctuations of the electrostatic potential $\tilde{\phi}$ normalized to the electron temperature T_e can be of the order of unity, as inferred from Eq. (4) and Eq. (6). In particular, we observe $\tilde{\phi}/T_e \lesssim 1$ at all radii with, for example, $\tilde{\phi} \sim 0.5$ and $T_e \sim 0.6$ for $r \lesssim r_s$.

In Fig. 8, we present snapshots of the vorticity for the $\mathbf{E} \times \mathbf{B}$ flow, which is described by the vorticity variable $\Omega = \nabla_{\perp}^2 \phi$, defined in Eq. (21), at the center of the device ($z = 0R$) at steady-state obtained in the case of the GM simulations with $(P, J) = (6, 1)$ in the LC and HC regimes. It is observed that the vorticity exhibits large perpendicular structures, i.e. $k_{\perp} \rho_{s0} \ll 1$, driven by the KH instability, which develop in the region of steep equilibrium gradients near $r \sim r_s$. These structures have slightly smaller amplitude away from r_s in all cases. Additionally, no clear differences are observed between the LC and HC regimes. Similar plots are obtained with the Braginskii and GM simulations. Finally, we note that further numerical investigations are necessary to verify the numerical resolution of the smallest perpendicular scale revealed by Fig. 8.

We now proceed to analyze the root mean square (RMS) of the fluctuations, defined as $\sqrt{\langle \tilde{n}_e^2 \rangle_t}$ in the case of the electron density fluctuations \tilde{n}_e (and similarly for the other quantities). Fig. 9 displays the RMS of the electron density, n_e , and the electrostatic potential, ϕ , fluctuations plotted as a function of the radius. The data are computed at $z = 0R$ and normalized to $\langle n_e \rangle_t(r)$ (and to $\langle \phi \rangle_t(r)$)^{33,37}. We find that the RMS values of the density displayed in Fig. 9 exhibit a qualitatively similar behaviour to those obtained in previous fluid simulations^{35,36} and GK simulations³⁷. Consistent with the observations made in Fig. 7, the RMS values reach their maximum when the gradients are most pronounced near $r \sim r_s$. For $r \lesssim r_s$ and for

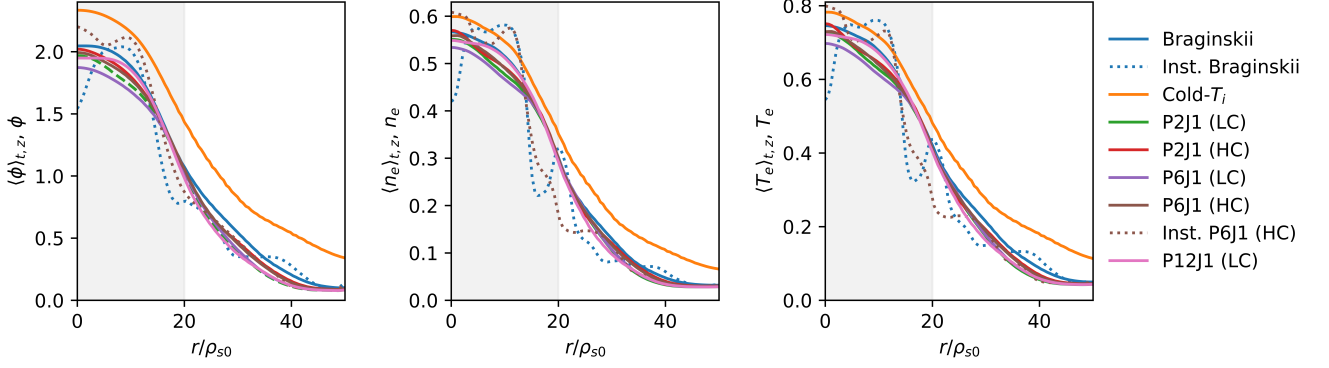


FIG. 4. Time-averaged profiles (solid colored lines) of the electrostatic potential $\langle \phi \rangle_{t,z}$ (left), electron density $\langle n_e \rangle_{t,z}$ (center), and electron temperature $\langle T_e \rangle_{t,z}$ (right) obtained in the GM simulations in the HC regime using $(P,J) = (2,1)$, $(6,1)$ and in the LC regime using $(P,J) = (2,1)$, $(6,1)$ and $(12,1)$, as a function of the radial coordinate r . The cold-ion and Braginskii simulations are also shown. The profiles are averaged over the region $-8R \leq z \leq 8R$. The instantaneous profiles are shown by the dotted colored lines for the Braginskii and $(P,J) = (6,1)$ GM in the HC regime simulations. The gray shaded areas represent the radial extent of the localized sources.

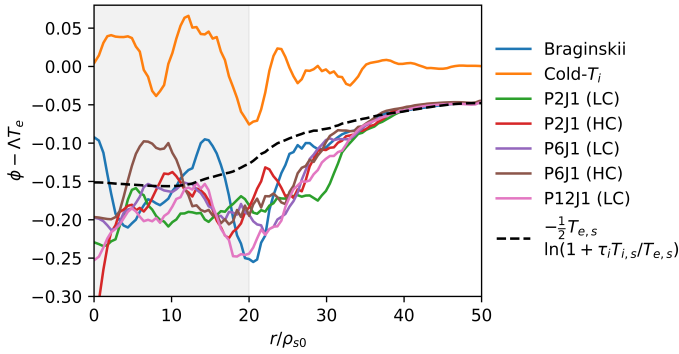


FIG. 5. Radial instantaneous profiles of the difference between ϕ and ΔT_e at $z = 0R$, in the LC and HC regimes for different number of GMs (P,J) and at quasi-steady state. The results from the cold-ion and Braginskii simulations are also shown. The black dotted line shows the value of $-\frac{1}{2}T_{e,s} \ln(1 + \tau_i T_{i,s}/T_{e,s})/2$ in the Braginskii simulation at $z = 0R$ (similar values of obtained in the GM simulations). The gray shaded area ($r \lesssim r_s$) represents the radial extent of the top-hat-like sources. For $r \gg r_s$, ϕ relaxes to ΔT_e .

$r \gtrsim r_s$ (where the gradients are smaller), the RMS values decrease because of the absence of the instability drive. Using a low number of GMs or considering the LC regime results in slightly larger RMS values (in particular of ϕ). Overall, this indicates that the level of fluctuations in the steep gradient region can be sensitive to the number of GMs used in the simulations. Finally, we note that the GM simulation with $(P,J) = (6,1)$ in the HC regime is the closest to the Braginskii predictions, and the largest RMS values (especially for \tilde{n}_e) are obtained in the cold-ion model.

We compare the RMS of the parallel electrical current J_{\parallel} measured at the sheath entrance located at $z = -18R$. The results are shown in Fig. 10 as a function of the radius and normalized to the maximum of $\langle J_{\parallel} \rangle_t(r)$. It is clearly observed that the boundary conditions imposed on the electron and ion

parallel velocities allow for the parallel current to fluctuate. This is in contrast to the case of logical sheath boundary condition, where $J_{\parallel} = 0$ is imposed everywhere⁶⁷. We remark that larger fluctuations of J_{\parallel} are obtained in the Braginskii simulations, while the largest RMS is observed in the case of the cold-ion model, a consequence of the finite ion temperature effect in the boundary conditions retained in the former (see Eq. (23)) and ignored in the later.

We now turn our attention to the skewness of the ion density fluctuations, which is defined as the third normalized moment of the electron density fluctuation, that is $\langle \tilde{n}_e^3 \rangle_t / \langle \tilde{n}_e^2 \rangle_t^{3/2}$. The skewness of the density is often used to characterize the dominance of plasma holes and blobs, associated with negative and positive skewness respectively^{33,35,36}. Fig. 11 shows the skewness of the electron density n_e . In all cases, the skewness is negative for $r \lesssim r_s$, indicating the presence of density holes in the region where the plasma source is present. On the other hand, in the region where $r \gtrsim r_s$, the skewness is positive. The sign and amplitude of the skewness shown in Fig. 11 have similar qualitative behaviour as in previous fluid³⁶ and GK^{37,38} simulations. In particular, the values obtained in the GM simulations are of the same order to those observed in the Braginskii case, albeit slightly smaller. Overall, the present turbulent analysis demonstrates that the full-F GM approach is in qualitative agreement with the Braginskii model, which is also employed in previous numerical investigations^{35,36} and validated with experimental data³³. We note that a more comprehensive analysis of turbulence, including aspects such as particle and energy transport, is necessary to evaluate the impact of velocity-space resolution and collisions (along with collision operator models) in greater detail. This analysis is deferred to future investigations, which would involve extending the present work to include FLR effects and removing the Boussinesq approximation, important for accurate turbulence transport predictions.

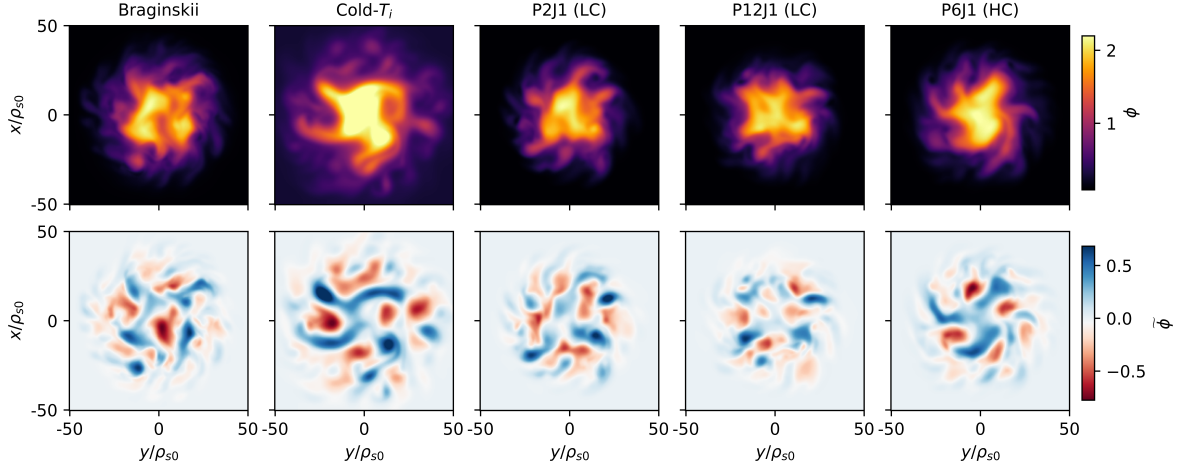


FIG. 6. Snapshots of the electrostatic potential ϕ (top) and of the fluctuations $\tilde{\phi} = \phi - \langle \phi \rangle_t$ (bottom) taken at $z = 0R$ obtained in the Braginskii, cold-ion (cold- T_i), $(P, J) = (2, 1)$, $(12, 1)$ in the LC regime, and $(P, J) = (6, 1)$ in the HC regime simulations (from left to right).

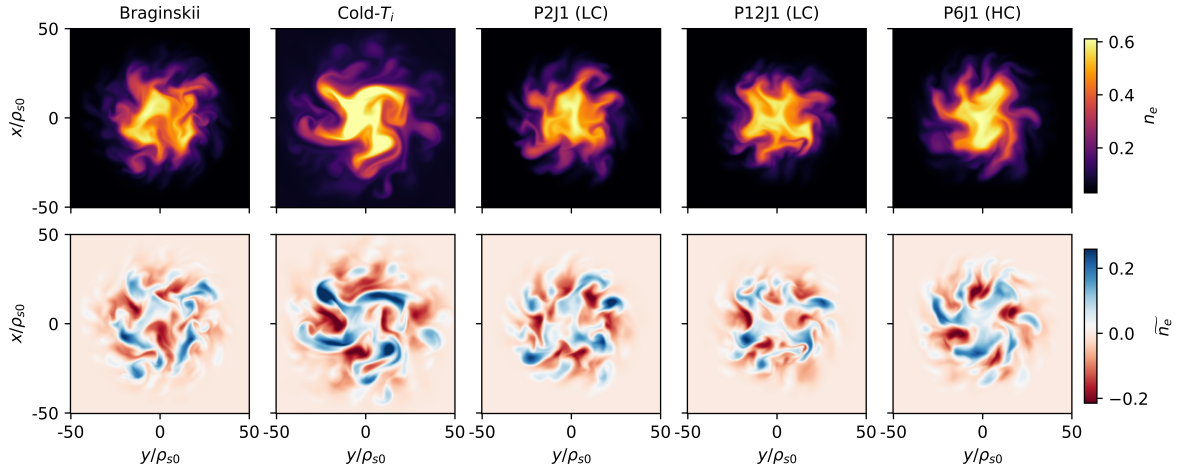


FIG. 7. Snapshots of the electron density n_e (top) and of the fluctuation $\tilde{n}_e = n_e - \langle n_e \rangle_t$ (bottom), similar to Fig. 6.

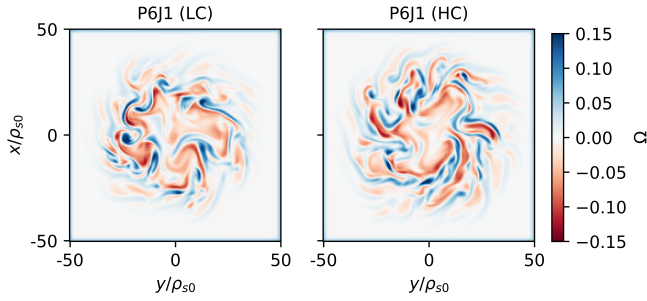


FIG. 8. Snapshots of the vorticity variable, Ω , obtained in the GM simulations with $(P, J) = (6, 1)$ in the LC (left) and HC (right) regimes at $z = 0R$.

C. Ion distribution function at quasi-steady state

We now investigate the features of the ion distribution function F_i in velocity-space. To obtain the full-F ion distribution function, F_i , from the GM simulations, we use the expansion in Eq. (8), truncated to a finite number of GMs, and we compute it as a function of x_i and the unshifted parallel coordinate, given by $v_{\parallel} / v_{Ti} = s_{\parallel i} + \sqrt{2\tau_i} U_{\parallel i}$. Also for this analysis, we consider the quasi-steady period. Figure. 12 shows F_i obtained from the $(P, J) = (6, 1)$ simulations in the HC and LC regime at the center of the machine ($z = 0R$) and at the sheath entrances, $z = -18R$ and $z = 18R$. At the two sheath entrances, F_i is centered around the ion parallel velocity, $U_i = \pm c_s$ respectively, a consequence of the Bohm sheath boundary conditions given in Eq. (23). On the other hand, F_i is centered around $v_{\parallel} \simeq 0$ at $z = 0R$, where $U_{\parallel i} \simeq 0$. The absence of fine velocity-space structures in Fig. 12 in both the HC and LC regimes confirms the weak dependence of turbulence prop-

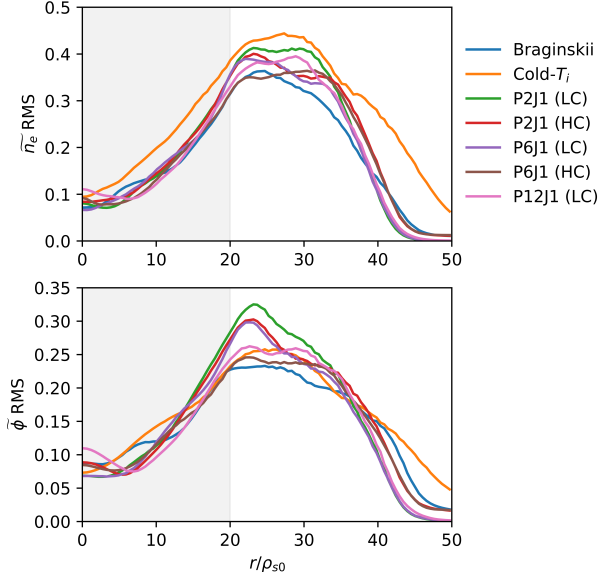


FIG. 9. RMS of the electron density n_e (normalized to $\langle n_e \rangle_i(r)$) (top) and electrostatic potential ϕ (normalized to $\langle \phi \rangle_i(r)$) (bottom) fluctuations (computed from Fig. 7 and Fig. 6) as a function of the radius r in the case of the Braginskii, cold-ion, and GM simulations at $z = 0R$. The shaded area indicates the radial extent of the sources.

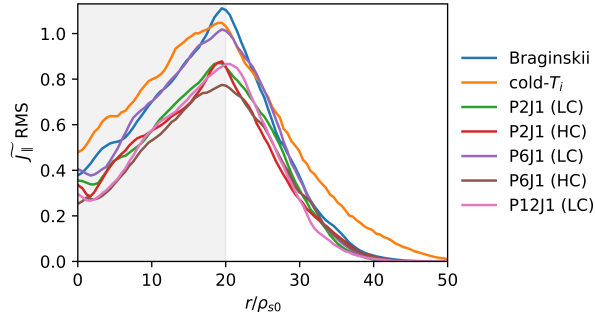


FIG. 10. RMS of the total parallel current J_{\parallel} (normalized to the maximum of $\langle J_{\parallel} \rangle_i(r)$) as a function of the radius at the sheath entrance near $z = -18R$.

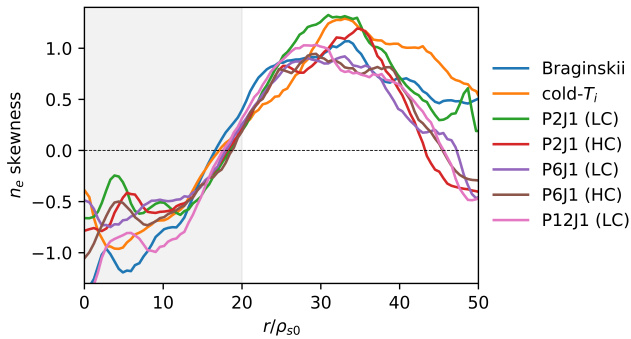


FIG. 11. Skewness of the electron density n_e as a function of r at $z = 0R$. The gray shaded area represents the radial extent of the sources.

erties on the number of GMs, as reported in Sec. IV B. In fact, fine velocity-space structures in F_i are not expected to play a significant role in LAPD due to the absence of magnetic drifts, trapped particles, of the high-collisional regime, and the fluid nature of the KH-dominated turbulent transport. Nevertheless, we remark that strong velocity-space gradients can appear near the sheath entrance in the electron distribution function (see, e.g., Ref. 38). The Maxwellian shape of F_i observed in our simulations is also consistent with the fact that both two-fluid Braginskii^{29,36} and GK^{37,38} simulations of LAPD yield qualitatively similar results.

Figure. 13 shows the ion distribution function at the sheath entrance ($z = 18R$ and $x = y = 0$) for $x_i = 0$, in the LC and HC regimes and for different values of (P, J) . We first observe that the bulk region of F_i (near $v_{\parallel}/v_{Ti} \sim 1$) is well approximated by a shifted Maxwellian. However, deviations from the Maxwellian distribution function are noticeable in the tails of F_i in the LC regime. These deviations become pronounced as (P, J) increases (e.g., from $(6, 1)$ to $(12, 1)$) which indicates that F_i is not sufficiently resolved in the LC regime. Finally, we remark that collisional effects tend to widen F_i due to the collisional parallel velocity-space diffusion present in the nonlinear Dougherty operator. We note that further convergence studies are required to fully evaluate the velocity-space resolution in Fig. 13 by considering a larger number of GMs than those considered in the present work, in particular in the LC regime.

The GM hierarchy equation in Eq. (12) does not enforce the positivity of the ion distribution function when evolving a finite number of GMs. For instance, the use of v_{\parallel}/v_{Ti} as an argument in the Hermite polynomials, H_p , in Eq. (8) would compromise the convergence properties of the GM approach, with respect to the use of v_{\parallel}/v_{Ti} , leading to simulations that show unphysical distribution functions with negative values when the same number of GMs are considered, as in the simulations presented here (Fig. 12 would show negative values). In fact, if the unshifted GMs $\mathcal{N}_{v_{\parallel}}^{pj}$, defined with respect to v_{\parallel}/v_{Ti} as the argument of H_p , i.e.

$$\mathcal{N}_{v_{\parallel}}^{pj} = 2\pi \int_{-\infty}^{\infty} dv_{\parallel} \int_0^{\infty} d\mu \frac{B}{m_i} F_i \frac{H_p\left(\frac{v_{\parallel}}{v_{Ti}}\right) L_j(x_i)}{\sqrt{2^p p!}}, \quad (25)$$

are used to expand F_i , it is found that $\mathcal{N}_{v_{\parallel}}^{pj} \neq 0$ for $(p, j) > 0$, even when F_i is a Maxwellian distribution function centered at $U_{\parallel i} \neq 0$. Indeed, using Eq. (25), one derives the analytical expression of the unshifted GMs for $F_i = F_{Mi}$,

$$\begin{aligned} \mathcal{N}_{v_{\parallel}}^{pj} &= \frac{\delta_j^0}{\sqrt{\pi}} \int_{-\infty}^{\infty} d\left(\frac{v_{\parallel}}{v_{Ti}}\right) e^{-(v_{\parallel}/v_{Ti} - U_{\parallel i}/(\sqrt{2}\tau_i))^2} \frac{H_p\left(\frac{v_{\parallel}}{v_{Ti}}\right)}{\sqrt{2^p p!}} \\ &= \sqrt{\frac{2^p}{p!}} \left(\frac{U_{\parallel i}}{\sqrt{2}\tau_i}\right)^p \delta_j^0, \end{aligned} \quad (26)$$

where $U_{\parallel i}$ is normalized to c_{s0} . While the amplitude of the unshifted GM decreases rapidly in the presence of subsonic ion

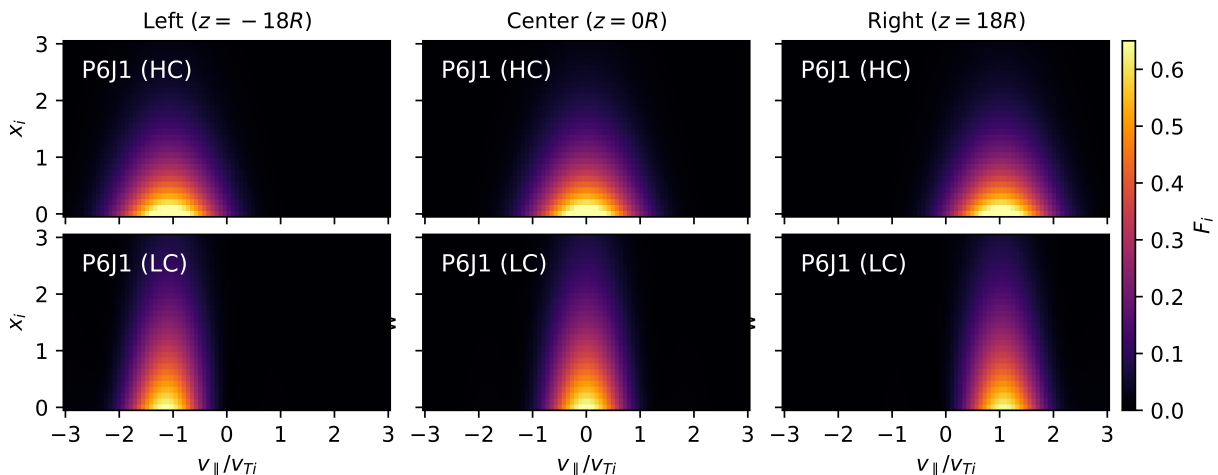


FIG. 12. Quasi-steady state ion distribution function, F_i , plotted as a function of $(v_{||}/v_{Ti}, x_i)$, obtained using $(P, J) = (6, 1)$ GMs in the HC regime (top) and LC regime (bottom). F_i is computed at the $z = -18R$ (left), $z = 0R$ (center), and $z = 18R$ (right) at the center in the perpendicular plane ($x = y = 0$).

flow, $U_{||i} \ll 1$, the decrease of the amplitude with p is slower in the presence of sonic flows, such that $\mathcal{N}_{v_{||}}^{pj} \sim \sqrt{2^p/p!}$.

D. GM spectrum at quasi-steady state

To better assess the velocity-space representation of F_i in our simulations, we plot the absolute value of the GMs, \mathcal{N}^{pj} (normalized to \mathcal{N}^{p0}), at the sheath entrance of the device, $z = 18R$ and $r = 0$, in Fig. 14. We consider the GMs associated with the distribution functions displayed in Fig. 13. As it can be clearly observed, the amplitude of the GMs decays faster in the HC regime than in the LC regime. In fact, extrapolating from linear theory in slab geometry¹², the amplitude of the GMs is expected to follow $|\mathcal{N}^{pj}| \sim \exp[-c_p(v_i)p^\alpha]$ in the $p \gg 1$ limit (with $c_p(v_i)$ a positive coefficient that increases with collisionality, v_i and $\alpha > 0$). While this estimate has been verified in linear studies and remains to be proven valid in full-F turbulent simulations, it provides us with a useful proxy for the expected decay of the GMs in the presence of collisions.

The results show that $P > 12$ would be required to ensure that F_i is sufficiently well resolved in the LC regime. Since the smaller relevance of the LC regime for the experimental parameters of LAPD, simulations with $P > 12$ have not been carried out in the present work to properly assess the velocity-space resolution of F_i . On the other hand, the contributions from \mathcal{N}^{p0} with $p \gtrsim 4$ are negligible in the HC regime, thereby justifying the closure by truncation for $P \gtrsim 4$. We also notice that $\mathcal{N}^{10} = 0$ in all cases, as a consequence of Eq. (11b). Finally, we note that the amplitude of the low-order GMs is not sensitive to P , as shown in Fig. 14. More precisely, the low-order GMs for $(P, J) = (6, 1)$ strongly resemble the ones of the $(P, J) = (12, 1)$ simulation in the LC case. This holds true also in the HC regime, for instance, by comparing the $(P, J) = (6, 1)$ and $(P, J) = (2, 1)$ simulations.

We also show in Fig. 14 that the amplitudes of the $j = 1$ GMs are smaller than the ones with $j = 0$. Numerical experiments (not shown) have also revealed that GMs with $j > 1$ have a negligible amplitude due to the absence of source for $j > 1$ and of FLR effects. This suggests (in addition to the similar results obtained in Sec. IV B with different (P, J)) that full-F turbulent calculations using the GM approach are less sensitive to the values of P and J than linear computations^{11,12}, where applying a closure by truncation at low P and J can introduce spurious artifacts¹³. Otherwise, Fig. 14 reveals that the slightly larger RMS values depicted in Fig. 9 (e.g., $(P, J) = (6, 1)$ in the LC and $(P, J) = (2, 1)$ in the HC regime) correspond to cases where the GM representation of F_i is unresolved. Additional investigations are required to verify the effect of closure in the presence of kinetic effects such as trapped particles and magnetic drifts, which are absent in LAPD, and of FLR effects, which are neglected in our model.

Finally, Fig. 15 presents snapshots of the GMs for different values of p in the perpendicular plane obtained for the $(P, J) = (6, 1)$ simulations in the LC and HC regimes. It is also visible that the turbulent structures are dominated by a long-wavelength perpendicular fluctuations for all values of p , which are driven by the KH instability. Indeed, the amplitude of these turbulent structures is strongly reduced if the nonlinear drive of the KH instability is artificially removed from our simulations. The decay of the amplitude of the turbulent structures due to collisions and with increasing p is also evident.

V. CONCLUSIONS

In this work, we present the first full-F turbulent simulations based on the GM approach using an arbitrary number of moments in a linear plasma device configuration with open straight field lines, such as LAPD. Neglecting FLR effects, we

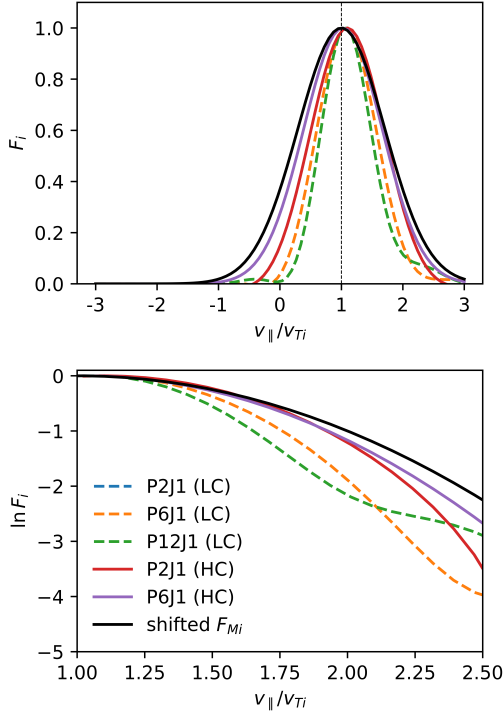


FIG. 13. Cuts of the ion distribution function F_i (normalized to its maximum) at $x_i = 0$ at the right sheath entrance near $z = 18R$ and $x = y = 0$ (top) for different (P, J) in the HC (solid lines) and LC (dotted lines) regimes, and close view over the region $v_{||}/v_{Ti} \in [1, 2.5]$ (bottom). The solid black line represents a Maxwellian distribution function shifted by the ion sound speed c_s (see Eq. (6)). A similar plot is obtained at the left sheath entrance ($z = -18R$).

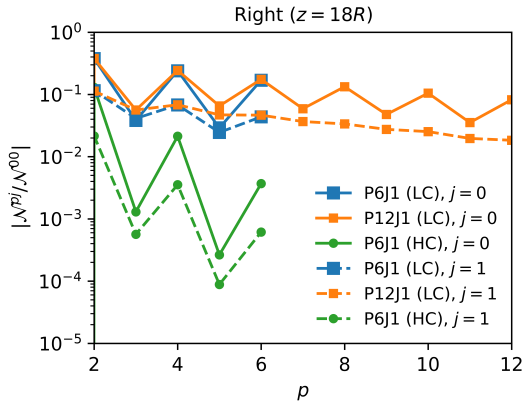


FIG. 14. Absolute value of the GMs \mathcal{N}^{pj} (normalized to \mathcal{N}^{00}) associated with the distribution functions shown in Fig. 13, plotted on a logarithmic scale as a function of $p \geq 2$ (solid lines for $j = 0$ and dashed lines for $j = 1$) obtained from different (P, J) simulations in the LC (square colored markers) and HC (circle colored markers) regime at $z = 18R$ and $x = y = 0$. The amplitude of the GM decreases with p in all cases and it is faster in the HC regime.

consider an electrostatic and long-wavelength ion GK model for the full ion distribution function F_i , coupled to the electron Braginskii fluid model for the electron density n_e , parallel velocity $U_{||e}$, and temperature T_e . The ion GK model is solved by deriving a full-F ion GM hierarchy equation, based on the Hermite-Laguerre polynomial expansion of F_i . In particular, a velocity-space coordinate centered at the local fluid ion parallel velocity is used to expand F_i , which ensures good convergence properties of the Hermite expansion in the presence of sonic ion flows. The GM hierarchy equation we consider is equivalent to the electrostatic and Boussinesq limits of the GK moment model for the boundary region derived in Ref. 10 with vanishing FLR effects. To account for the parallel losses at the end plates, Bohm sheath boundary conditions are used, equivalent to those previously used in LAPD fluid simulations²⁹. A nonlinear ion-ion Dougherty collision operator is also considered. The ion GM hierarchy equation with the fluid electron model is implemented in a numerical code, allowing us to perform the first full-F turbulent calculations based on a moment approach with a flexible number of GMs. This is in contrast to previous full-F gyrofluid simulations where the number of moments is fixed⁴⁶⁻⁴⁸.

We present the simulations of a linear device using LAPD physical parameters based on a Helium plasma²⁹ and a first-of-the-kind comparison with the two-fluid Braginskii model. Several nonlinear simulations are performed using a different number of Hermite and Laguerre GMs in a low and high-collisional ion regime. Overall, a qualitative agreement on the time-averaged radial profiles between the Braginskii model and the GM approach is observed. This is expected from our analysis which shows that turbulence is dominated by the long perpendicular wavelength and $k_{||} \simeq 0$ Kelvin-Helmholtz instability of fluid nature.

The RMS and skewness of the fluctuations in the GM simulations also agree with the ones previously obtained in fluid^{29,35} and GK^{37,38} simulations of LAPD. In particular, we find that the RMS values are often larger than the ones predicted by the Braginskii model, if the number of GMs is not sufficient to properly resolve the ion distribution function. The largest RMS values are observed with the cold-ion reduced model (with a difference up to $\sim 20\%$ with respect to the Braginskii model), while the results closest to the one of the Braginskii model are obtained if collisions are introduced in the GM approach with a sufficient number of GMs, in this case $(P, J) = (6, 1)$. Overall, collisions reduce slightly the turbulent fluctuations level, but they do not significantly alter the observed turbulent regimes. At the same time, the analysis of the ion distribution function F_i reveals that collisions damp the amplitudes of the GMs, thereby allowing for a reduction in the number of GMs required in the simulations (typically from $(P, J) \sim (12, 1)$ in the low collisional regime to $(P, J) \sim (6, 1)$ in the high-collisional regime of LAPD).

We note that although the present work allows the simulation of LAPD with a flexible number of GMs, unlike previous full-F gyrofluid simulations⁴⁶⁻⁴⁸, improvements in our physical model are required to increase the fidelity of our simulations. For example, the inclusion of FLR effects^{50,51} is necessary to study small scale fluctuations. A more de-

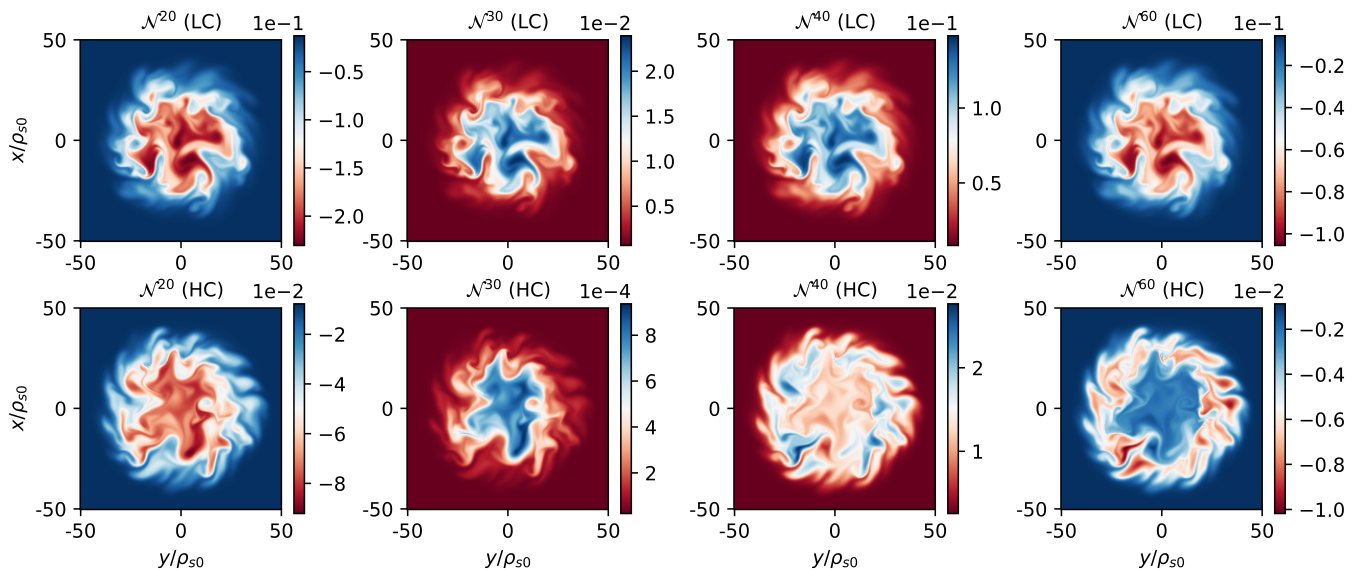


FIG. 15. Instantaneous snapshots of the GMs \mathcal{N}^{pj} , with $p = 2, 3, 4, 6$ and $j = 0$, in the (x, y) perpendicular plane at the sheath entrance located at $z = 18R$ from the $(P, J) = (6, 1)$ simulations in the LC (top) and HC (bottom) regime. The large perpendicular structures are caused by the KH instability.

tailed study of the role of FLR effects is the subject of future work. Incorporating FLR effects with a flexible number of GMs necessitates conducting comprehensive numerical investigations to evaluate the impact of the numerical and velocity-space resolution on turbulent structures, in particular at small scales, supported by the examination of conservation laws, an aspect not explored in the present work. In addition, a more accurate description of the role of collisions requires the implementation of a nonlinear collision operator model with increasing physical fidelity, such as the nonlinear Coulomb operator¹⁴. Proper sheath boundary conditions for the GM hierarchy equation, which extend the simplified Bohm sheath boundary condition used here (see Eq. (23)), can improve the reliability of our simulations. These boundary conditions can be obtained by a procedure similar to that described in Ref. 31. Finally, we note that the implementation of a kinetic electron description is also essential to perform high-fidelity LAPD simulations, since fast and less collisional electrons (with $T_e \sim 15$ eV) are emitted by pulsed plasma discharges in experiments⁶⁸. Furthermore, kinetic electrons are important in setting the sheath boundary conditions where electrons are reflected due to the potential drop, giving rise to strong speed-space gradients in the electron distribution function³⁸.

More generally, the present work represents a step towards the development of future full-F turbulent simulations of the boundary region of fusion devices using the GM approach with a flexible number of GMs, which may provide an ideal flexible tool to capture kinetic and collisional effects at the desired level of accuracy.

ACKNOWLEDGEMENT

The authors acknowledge helpful discussions with Alessandro Geraldini and Stephan Brunner. This work has been carried out within the framework of the EUROfusion Consortium, via the Euratom Research and Training Programme (Grant Agreement No 101052200 — EUROfusion) and funded by the Swiss State Secretariat for Education, Research and Innovation (SERI). Views and opinions expressed are however those of the author(s) only and do not necessarily reflect those of the European Union, the European Commission, or SERI. Neither the European Union nor the European Commission nor SERI can be held responsible for them. The simulations presented herein were carried out in part on the CINECA Marconi supercomputer under the TSVVT422 project and in part at CSCS (Swiss National Supercomputing Center). This work was supported in part by the Swiss National Science Foundation.

Appendix A: High-collisional limit of ion temperature equation

In this appendix, we derive the Braginskii equation for the ion temperature T_i , given Eq. (22b), from the ion GM hierarchy equation provided in Eq. (12). This allows us to elucidate the relationship between the GM approach and the Braginskii model, particularly in the high-collisional regime, and to justify the terms on the right-hand side of Eq. (22b).

First, we note that since our model neglects FLR effects, the gyrocenter quantities are assumed to be equal to the particle fluid quantities. Hence, the time evolution of the ion temperature T_i can be expressed in terms of GMs using the definitions of the gyrocenter fluid quantities in Eq. (11). Evaluating the

time derivative of T_i yields

$$N_i \partial_t T_i = \frac{\sqrt{2}}{3} \partial_t \mathcal{N}^{20} - \frac{2}{3} \partial_t \mathcal{N}^{01} + (1 - T_i) \partial_t N_i. \quad (\text{A1})$$

The time derivatives of the GMs contained in Eq. (A1) can be evaluated using the ion GM hierarchy equation given in Eq. (12) with $(p, j) = (2, 0)$ and $(0, 1)$. We obtain

$$\begin{aligned} \partial_t \mathcal{N}^{20} = & -\sqrt{\tau_i} \partial_z \sqrt{3} \mathcal{N}^{30} - \partial_z (U_{\parallel i} \mathcal{N}^{20}) - \frac{1}{\rho_*} [\phi, \mathcal{N}^{20}] \\ & - \left(2 \mathcal{N}^{20} + \sqrt{2} \mathcal{N}^{00} \right) \partial_z U_{\parallel i} + \mathcal{C}_i^{20} + S_{\mathcal{E}}^{20}, \end{aligned} \quad (\text{A2a})$$

$$\begin{aligned} \partial_t \mathcal{N}^{01} = & -\sqrt{\tau_i} \partial_z \mathcal{N}^{11} - \partial_z (U_{\parallel i} \mathcal{N}^{01}) - \frac{1}{\rho_*} [\phi, \mathcal{N}^{01}] \\ & + \mathcal{C}_i^{01} + S_{\mathcal{E}}^{01}. \end{aligned} \quad (\text{A2b})$$

Using Eq. (A2) with the ion continuity equation given in Eq. (17a) into Eq. (A1), we derive

$$\begin{aligned} N_i \partial_t T_i = & -\frac{\sqrt{2} \tau_i}{3} \partial_z \left(\sqrt{3} \mathcal{N}^{30} - \sqrt{2} \mathcal{N}^{11} \right) \\ & - U_{\parallel i} N_i \partial_z T_i - \frac{N_i}{\rho_*} [\phi, T_i] - \frac{2}{3} P_{\parallel i} \partial_z U_{\parallel i} \\ & + S_{\mathcal{E}} + (1 - T_i) S_{\mathcal{N}}, \end{aligned} \quad (\text{A3})$$

where the collision terms, \mathcal{C}_i^{20} and \mathcal{C}_i^{01} , cancel out due to the energy conservation of the collision operator (see Eq. (15)). In addition, the definitions of the sources given in Eq. (14) are used to derive the last terms on the right-hand side of Eq. (A3).

We now use the fact that FLR effect are neglected in our model such that $N_i \simeq n_e$. Moreover, an expression for the parallel gradient of the parallel ion flow, $\partial_z U_{\parallel i}$, can be obtained from the vorticity equation given in Eq. (22c). At the leading-order in the long-wavelength limit, one finds that $\partial_z J_{\parallel} \simeq 0$, such that

$$N_i \partial_z U_{\parallel i} \simeq (U_{\parallel e} - U_{\parallel i}) \partial_z n_e + n_e \partial_z U_{\parallel e}. \quad (\text{A4})$$

Finally, introducing the normalized parallel ion heat flux,

$$q_{\parallel i} = \sqrt{2} \tau_i \left(\frac{\sqrt{3}}{2} \mathcal{N}^{30} - \frac{\mathcal{N}^{11}}{\sqrt{2}} \right), \quad (\text{A5})$$

and using Eq. (A4), the ion temperature equation Eq. (A3) becomes

$$\begin{aligned} \partial_t T_i + \frac{1}{\rho_*} [\phi, T_i] + U_{\parallel i} \partial_z T_i = & + \frac{2}{3} T_i \left[(U_{\parallel i} - U_{\parallel e}) \frac{\partial_z n_e}{n_e} - \partial_z U_{\parallel e} \right] \\ & - \frac{2}{3} \frac{1}{n_e} \partial_z q_{\parallel i} + \frac{A_{\mathcal{E}}}{n_e} + (1 - T_i) \frac{S_{\mathcal{N}}}{n_e}. \end{aligned} \quad (\text{A6})$$

We remark that Eq. (A6) can also be deduced from other full-F gyrofluid models^{45,48}, which consider finite ion temperature effects with a fixed number of GMs. To close Eq. (A6), an expression for the parallel ion heat flux $q_{\parallel i}$ must be prescribed. In contrast to the ion GM hierarchy equation, which treats the ion parallel heat flux $q_{\parallel i}$ as a dynamical variable by evolving high-order GMs (see Eq. (A5)), the Braginskii model assumes a high-collisional limit (where $\lambda_{mpf} k_{\parallel} \ll 1$), allowing for the derivation of a collisional closure for $q_{\parallel i}$. Specifically, using the Fokker-Planck collision operator and applying the high-collisional closure via the Chapman-Enskog procedure^{52,69,70}, we can obtain the fluid closure $q_{\parallel i} \simeq -\chi_{\parallel} \partial_z T_i$, where χ_{\parallel} represents the normalized parallel ion thermal conductivity predicted by the Braginskii transport equation^{9,70}. Hence, in the high-collisional limit, the ion temperature equation Eq. (A6) reduces to

$$\begin{aligned} \partial_t T_i + \frac{1}{\rho_*} [\phi, T_i] + U_{\parallel i} \partial_z T_i = & + \frac{2}{3} T_i \left[(U_{\parallel i} - U_{\parallel e}) \frac{\partial_z n_e}{n_e} - \partial_z U_{\parallel e} \right] \\ & + \partial_z (\chi_{\parallel i} \partial_z T_i) + \frac{A_{\mathcal{E}}}{n_e} + (1 - T_i) \frac{S_{\mathcal{N}}}{n_e}, \end{aligned} \quad (\text{A7})$$

where the temperature anisotropy is neglected such that $T_{\parallel i} \simeq T_i$ at high-collisionality¹². Hence, Eq. (A7) is equivalent to the ion temperature equation given in Eq. (22b) used in the Braginskii model where the source terms are due to the density and energy sources (see Eq. (14)) considered in the ion GM hierarchy equation.

A high-collisional closure for the parallel ion heat flux can also be derived using the Dougherty collision operator (or other collision operator models). However, it has been shown that simplified collision operators can lead to large deviations (with respect to the Fokker-Planck collision operator) in the predictions of the conductivities¹⁶, especially when using operators like Dougherty, as in this work.

Finally, it is worth noting that, while the Braginskii collisional closure diverges in the low-collisionality limit⁷¹, resulting in an overestimate of the parallel heat flux, the GM hierarchy equation allows for the evolution of $q_{\parallel i}$ using a larger number of GMs. However, while this effect may not be as significant in LAPD due to the low temperature, it could be more pronounced in the boundary region.

¹M. Dorf and M. Dorr, "Progress with the 5D full-F continuum gyrokinetic code COGENT," *Contributions to Plasma Physics* **60**, e201900113 (2020).

²A. H. Hakim, N. R. Mandell, T. N. Bernard, M. Francisquez, G. W. Hammett, and E. L. Shi, "Continuum electromagnetic gyrokinetic simulations of turbulence in the tokamak scrape-off layer and laboratory devices," *Physics of Plasmas* **27**, 042304 (2020).

³D. Michels, P. Ulbl, W. Zholobenko, T. Body, A. Stegmeir, T. Eich, M. Griener, G. D. Conway, F. Jenko, and A. U. Team, "Full-f electromagnetic gyrokinetic turbulence simulations of the edge and scrape-off layer of ASDEX Upgrade with GENE-X," *Physics of Plasmas* **29**, 032307 (2022).

⁴P. Ulbl, T. Body, W. Zholobenko, A. Stegmeir, J. Pfennig, and F. Jenko, "Influence of collisions on the validation of global gyrokinetic simulations in the edge and scrape-off layer of TCV," *Physics of Plasmas* **30** (2023).

⁵C. S. Chang, S. Ku, A. Loarte, V. Parail, F. Koechl, M. Romanelli, R. Maingi, J.-W. Ahn, T. Gray, J. Hughes, *et al.*, "Gyrokinetic projection

- of the divertor heat-flux width from present tokamaks to ITER,” *Nuclear Fusion* **57**, 116023 (2017).
- ⁶A. Stegmeir, D. Coster, A. Ross, O. Maj, K. Lackner, and E. Poli, “GRILLIX: a 3D turbulence code based on the flux-coordinate independent approach,” *Plasma Physics and Controlled Fusion* **60**, 035005 (2018).
- ⁷D. S. De Oliveira, T. A. Body, D. Galassi, C. Theiler, E. Laribi, P. Tamain, A. Stegmeir, M. Giacomini, W. Zholobenko, P. Ricci, *et al.*, “Validation of edge turbulence codes against the TCV-X21 diverted L-mode reference case,” *Nuclear Fusion* **62**, 096001 (2022).
- ⁸M. Giacomini, P. Ricci, A. Coroado, G. Fourestey, D. Galassi, E. Lanti, D. Mancini, N. Richart, L. N. Stenger, and N. Varini, “The gbs code for the self-consistent simulation of plasma turbulence and kinetic neutral dynamics in the tokamak boundary,” *Journal of Computational Physics*, 111294 (2022).
- ⁹A. Zeiler, J. F. Drake, and B. Rogers, “Nonlinear reduced braginskii equations with ion thermal dynamics in toroidal plasma,” *Physics of Plasmas* **4**, 2134 (1997).
- ¹⁰B. J. Frei, R. Jorge, and P. Ricci, “A gyrokinetic model for the plasma periphery of tokamak devices,” *Journal of Plasma Physics* **86**, 905860205 (2020).
- ¹¹R. Jorge, P. Ricci, S. Brunner, S. Gamba, V. Konovets, N. F. Loureiro, L. M. Perrone, and N. Teixeira, “Linear theory of electron-plasma waves at arbitrary collisionality,” *Journal of Plasma Physics* **85**, 905850211 (2019).
- ¹²B. J. Frei, A. C. D. Hoffmann, and P. Ricci, “Local gyrokinetic collisional theory of the ion-temperature gradient mode,” *Journal of Plasma Physics* **88**, 905880304 (2022).
- ¹³B. J. Frei, A. C. D. Hoffmann, P. Ricci, S. Brunner, and Z. Tecchioll, “Moment-based approach to the flux-tube linear gyrokinetic model,” *Journal of Plasma Physics* **89**, 905890414 (2023).
- ¹⁴R. Jorge, B. J. Frei, and P. Ricci, “Nonlinear gyrokinetic Coulomb collision operator,” *Journal of Plasma Physics* **85**, 905850604 (2019).
- ¹⁵B. J. Frei, J. Ball, A. C. D. Hoffmann, R. Jorge, P. Ricci, and L. Stenger, “Development of advanced linearized gyrokinetic collision operators using a moment approach,” *Journal of Plasma Physics* **87**, 905870501 (2021).
- ¹⁶B. J. Frei, S. Ernst, and P. Ricci, “Numerical implementation of the improved sugama collision operator using a moment approach,” *Physics of Plasmas* **29**, 093902 (2022).
- ¹⁷A. C. D. Hoffmann, B. J. Frei, and P. Ricci, “Gyrokinetic simulations of plasma turbulence in a z-pinch using a moment-based approach and advanced collision operators,” *Journal of Plasma Physics* **89**, 905890214 (2023).
- ¹⁸G. W. Hammett and F. W. Perkins, “Fluid moment models for Landau damping with application to the ion-temperature-gradient instability,” *Physical Review Letters* **64**, 3019 (1990).
- ¹⁹M. A. Beer and G. W. Hammett, “Toroidal gyrofluid equations for simulations of tokamak turbulence,” *Physics of Plasmas* **3**, 4046 (1996).
- ²⁰A. J. Brizard and T. S. Hahm, “Foundations of nonlinear gyrokinetic theory,” *Reviews of Modern Physics* **79**, 421 (2007).
- ²¹A. C. D. Hoffmann, B. J. Frei, and P. Ricci, “Dimits shift and impact of collisions using a gyrokinetic moment-based approach,” *arXiv preprint arXiv:2308.01016* (2023).
- ²²N. R. Mandell, W. Dorland, and M. Landreman, “Laguerre–Hermite pseudo-spectral velocity formulation of gyrokinetics,” *Journal of Plasma Physics* **84**, 905840108 (2018).
- ²³N. Mandell, W. Dorland, I. Abel, R. Gaur, P. Kim, M. Martin, and T. Qian, “GX: a GPU-native gyrokinetic turbulence code for tokamaks and stellarators,” *arXiv:2209.06731* (2022).
- ²⁴W. Gekelman, H. Pfister, Z. Lucky, J. Bamber, D. Leneman, and J. Maggs, “Design, construction, and properties of the large plasma research device–The LAPD at UCLA,” *Review of scientific instruments* **62**, 2875 (1991).
- ²⁵M. Gilmore, A. G. Lynn, T. R. Desjardins, Y. Zhang, C. Watts, S. C. Hsu, S. Betts, R. Kelly, and E. Schamiloglu, “The helcat basic plasma science device,” *Journal of Plasma Physics* **81**, 345810104 (2015).
- ²⁶I. Furno, R. Agnello, U. Fantz, A. Howling, R. Jacquier, C. Marini, G. Plyushchev, P. Guittienne, and A. Simonin, “Helicon wave-generated plasmas for negative ion beams for fusion,” in *EPJ Web of Conferences*, Vol. 157 (EDP Sciences, 2017) p. 03014.
- ²⁷G. R. Tynan, M. J. Burin, C. Holland, G. Antar, N. Crocker, and P. H. Diamond, “Radially sheared azimuthal flows and turbulent transport in a cylindrical plasma,” *Physics of plasmas* **11**, 5195 (2004).
- ²⁸O. F. Castellanos, E. Anabitarte, J. M. Senties, C. Hidalgo, and M. A. Pedrosa, “Parallel flows and turbulence in a linear plasma machine,” *Plasma Physics and Controlled Fusion* **47**, 2067 (2005).
- ²⁹B. N. Rogers and P. Ricci, “Low-frequency turbulence in a linear magnetized plasma,” *Physical Review Letters* **104**, 225002 (2010).
- ³⁰R. Chodura, “Plasma–wall transition in an oblique magnetic field,” *The Physics of Fluids* **25**, 1628 (1982).
- ³¹J. Loizu, P. Ricci, F. D. Halpern, and S. Jolliet, “Boundary conditions for plasma fluid models at the magnetic presheath entrance,” *Physics of Plasmas* **19**, 122307 (2012).
- ³²A. Geraldini, F. I. Parra, and F. Militello, “Gyrokinetic treatment of a grazing angle magnetic presheath,” *Plasma Physics and Controlled Fusion* **59**, 025015 (2017).
- ³³B. Friedman, T. A. Carter, M. V. Umansky, D. Schaffner, and B. Dudson, “Energy dynamics in a simulation of lapd turbulence,” *Physics of Plasmas* **19**, 102307 (2012).
- ³⁴P. Popovich, M. V. Umansky, T. A. Carter, and B. Friedman, “Modeling of plasma turbulence and transport in the large plasma device,” *Physics of Plasmas* **17**, 122312 (2010).
- ³⁵D. M. Fisher, B. N. Rogers, G. D. Rossi, D. S. Guice, and T. A. Carter, “Three-dimensional two-fluid braginskii simulations of the large plasma device,” *Physics of Plasmas* **22**, 092121 (2015).
- ³⁶A. Ross, A. Stegmeir, P. Manz, D. Groselj, W. Zholobenko, D. Coster, and F. Jenko, “On the nature of blob propagation and generation in the large plasma device: Global grillix studies,” *Physics of Plasmas* **26**, 102308 (2019).
- ³⁷E. L. Shi, G. W. Hammett, T. Stoltzfus-Dueck, and A. Hakim, “Gyrokinetic continuum simulation of turbulence in a straight open-field-line plasma,” *Journal of Plasma Physics* **83**, 905830304 (2017).
- ³⁸Q. Pan, D. Told, E. Shi, G. W. Hammett, and F. Jenko, “Full-f version of GENE for turbulence in open-field-line systems,” *Physics of Plasmas* **062303**, 1 (2018).
- ³⁹J. P. Dougherty, “Model Fokker-Planck equation for a plasma and its solution,” *The Physics of Fluids* **7**, 1788 (1964).
- ⁴⁰T. A. Carter, “Intermittent turbulence and turbulent structures in a linear magnetized plasma,” *Physics of Plasmas* **13**, 010701 (2006).
- ⁴¹A. J. Brizard, “Nonlinear gyrofluid description of turbulent magnetized plasmas,” *Physics of Fluids B: Plasma Physics* **4**, 1213 (1992).
- ⁴²P. B. Snyder and G. W. Hammett, “A landau fluid model for electromagnetic plasma microturbulence,” *Physics of Plasmas* **8**, 3199 (2001).
- ⁴³D. Strintzi and B. Scott, “Nonlocal nonlinear electrostatic gyrofluid equations,” *Physics of plasmas* **11**, 5452 (2004).
- ⁴⁴J. Madsen, “Full-f gyrofluid model,” *Physics of Plasmas* **20**, 072301 (2013).
- ⁴⁵M. Held, M. Wiesenberger, J. Madsen, and A. Kendl, “The influence of temperature dynamics and dynamic finite ion larmor radius effects on seeded high amplitude plasma blobs,” *Nuclear Fusion* **56**, 126005 (2016).
- ⁴⁶M. Wiesenberger, L. Einkemmer, M. Held, A. Gutierrez-Milla, X. Sáez, and R. Iakymchuk, “Reproducibility, accuracy and performance of the feltor code and library on parallel computer architectures,” *Computer Physics Communications* **238**, 145 (2019).
- ⁴⁷D. Galassi, C. Theiler, T. Body, F. Manke, P. Micheletti, J. Omotani, M. Wiesenberger, M. Baquero-Ruiz, I. Furno, M. Giacomini, *et al.*, “Validation of edge turbulence codes in a magnetic x-point scenario in torpex,” *Physics of Plasmas* **29** (2022).
- ⁴⁸M. Wiesenberger and M. Held, “Long-wavelength closures for collisional and neutral interaction terms in gyro-fluid models,” *Journal of Physics: Conference Series* **2397**, 012015 (2022).
- ⁴⁹M. Wiesenberger and M. Held, “Effects of plasma resistivity in three-dimensional full-f gyro-fluid turbulence simulations,” *arXiv preprint arXiv:2309.10414* (2023).
- ⁵⁰M. Held, M. Wiesenberger, and A. Kendl, “Padé-based arbitrary wavelength polarization closures for full-F gyro-kinetic and-fluid models,” *Nuclear Fusion* **60**, 066014 (2020).
- ⁵¹M. Held and M. Wiesenberger, “Beyond the oberbeck–boussinesq and long wavelength approximation,” *Nuclear Fusion* **63**, 026008 (2022).
- ⁵²R. Jorge, P. Ricci, and N. F. Loureiro, “A drift-kinetic analytical model for scrape-off layer plasma dynamics at arbitrary collisionality,” *Journal of Plasma Physics* **83**, 905830606 (2017).
- ⁵³T. Goerler, X. Lapillonne, S. Brunner, T. Dannert, F. Jenko, F. Merz, and D. Told, “The global version of the gyrokinetic turbulence code GENE,”

- Journal of Computational Physics **230**, 7053 (2011).
- ⁵⁴Y. Sarazin, V. Grandgirard, J. Abiteboul, S. Allfrey, X. Garbet, P. Ghendrih, G. Latu, A. Strugarek, and G. Dif-Pradalier, “Large scale dynamics in flux driven gyrokinetic turbulence,” *Nuclear Fusion* **50**, 054004 (2010).
- ⁵⁵S. K. P. Tripathi, P. Pribyl, and W. Gekelman, “Development of a radio-frequency ion beam source for fast-ion studies on the large plasma device,” *Review of Scientific Instruments* **82**, 093501 (2011).
- ⁵⁶I. S. Gradshteyn and I. M. Ryzhik, *Table of integrals, series, and products* (Academic press, 2014).
- ⁵⁷M. Wiesenberger and M. Held, “Angular momentum and rotational energy of mean flows in toroidal magnetic fields,” *Nuclear Fusion* **60**, 096018 (2020).
- ⁵⁸G. Q. Yu, S. I. Krasheninnikov, and P. N. Guzdar, “Two-dimensional modelling of blob dynamics in tokamak edge plasmas,” *Physics of Plasmas* **13**, 042508 (2006).
- ⁵⁹K. Bodi, G. Ciraolo, F. Schwander, and E. Serre, “Impact of the boussinesq approximation in tokamak scrape-off layer turbulence,” in *38th Conference on Plasma Physics*, Vol. 1 (2011) p. 121.
- ⁶⁰P. Paruta, P. Ricci, F. Riva, C. Wersal, C. Beadle, and B. Frei, “Simulation of plasma turbulence in the periphery of diverted tokamak by using the GBS code,” *Physics of Plasmas* **25**, 112301 (2018).
- ⁶¹P. C. Stangeby, “The bohm–chodura plasma sheath criterion,” *Physics of Plasmas* **2**, 702 (1995).
- ⁶²A. Masetto, F. D. Halpern, S. Jolliet, J. Loizu, and P. Ricci, “Finite ion temperature effects on scrape-off layer turbulence,” *Physics of Plasmas* **22**, 012308 (2015).
- ⁶³K.-U. Riemann, “Kinetic theory of the plasma sheath transition in a weakly ionized plasma,” *The Physics of Fluids* **24**, 2163 (1981).
- ⁶⁴S. D. Baalrud, B. Scheiner, B. Yee, M. Hopkins, and E. Barnat, “Extensions and applications of the Bohm criterion,” *Plasma Physics and Controlled Fusion* **57**, 0444003 (2015).
- ⁶⁵R. M. Churchill, J. M. Canik, C. S. Chang, R. Hager, A. W. Leonard, R. Maingi, R. Nazikian, and D. P. Stotler, “Kinetic simulations of scrape-off layer physics in the DIII-D tokamak,” *Nuclear Materials and Energy* **12**, 978 (2017).
- ⁶⁶A. Arakawa, “Computational design for long-term numerical integration of the equations of fluid motion: Two-dimensional incompressible flow. Part I,” *Journal of computational physics* **135**, 103 (1997).
- ⁶⁷S. E. Parker, R. J. Procassini, C. K. Birdsall, and B. I. Cohen, “A suitable boundary condition for bounded plasma simulation without sheath resolution,” *Journal of Computational Physics* **104**, 41 (1993).
- ⁶⁸W. Gekelman, P. Pribyl, Z. Lucky, M. Drandell, D. Leneman, J. Maggs, S. Vincena, B. Van Compernelle, S. K. P. Tripathi, G. Morales, *et al.*, “The upgraded large plasma device, a machine for studying frontier basic plasma physics,” *Review of Scientific Instruments* **87**, 025105 (2016).
- ⁶⁹S. Chapman and T. G. Cowling, “The velocity of diffusion in a mixed gas; the second approximation,” *Proceedings of the Royal Society of London. Series A. Mathematical and Physical Sciences* **179**, 159 (1941).
- ⁷⁰S. I. Braginskii, “Transport processes in a plasma,” *Reviews of plasma physics* **1**, 205 (1965).
- ⁷¹C. Pitzal, A. Stegmeir, W. Zholobenko, K. Zhang, and F. Jenko, “Landau-fluid simulations of edge-SOL turbulence with GRILLIX,” *Physics of Plasmas* **30**, 122502 (2023).